

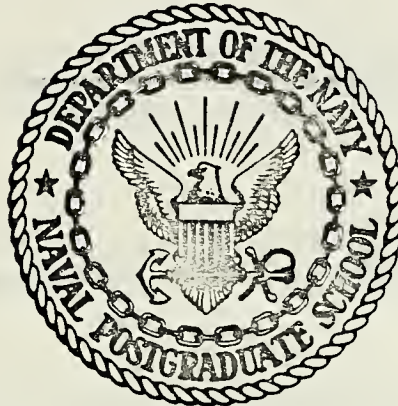
HYDRAULIC RAM SHOCK PHASE EFFECTS  
ON FUEL CELL SURVIVABILITY

Leslie George Kappel



# NAVAL POSTGRADUATE SCHOOL

## Monterey, California



# THESIS

HYDRAULIC RAM SHOCK PHASE EFFECTS  
ON FUEL CELL SURVIVABILITY

by

Leslie George Kappel

Thesis Advisor:

H. L. Power, Jr.

March 1974

T160122

*Approved for public release; distribution unlimited.*



Hydraulic Ram Shock Phase Effects  
on Fuel Cell Survivability

by

Leslie George Kappel  
Lieutenant, United States Navy  
B.S., Miami University (Ohio), 1966

Submitted in partial fulfillment of the  
requirements for the degree of

MASTER OF SCIENCE IN AERONAUTICAL ENGINEERING

from the

NAVAL POSTGRADUATE SCHOOL  
March 1974

---



## ABSTRACT

Hydraulic ram concerns the dynamic loading and catastrophic failure of liquid filled fuel tanks impacted by high speed projectiles. Hydraulic ram is divided into two phases: shock phase and cavity phase. The shock phase was studied. Theoretical predictions of shock radius versus time were compared with experimental results. The theory was found to be reasonably accurate for blunt shaped projectiles.

Included in the theory were predictions of shock pressure and pressure profiles behind the shock. Theoretical pressures are presented graphically but were not validated by experiment.

Velocity decay of the projectiles in the liquid was investigated and correlated with theory to provide information for further studies of the cavity phase.





## TABLE OF CONTENTS

I.	INTRODUCTION -----	8
II.	ANALYTICAL STUDY -----	11
	A. SHOCK FRONT PRESSURES -----	12
	B. PRESSURE FIELD BEHIND THE SHOCK -----	13
	C. SHOCK MACH NUMBER -----	15
III.	EXPERIMENTAL PROCEDURE -----	17
IV.	RESULTS AND CONCLUSIONS -----	31
	A. SHOCK RADIUS VERSUS TIME - PRE-PUNCHED FRONT WALL -----	31
	B. SHOCK RADIUS VERSUS TIME - SOLID FRONT WALL ---	37
	C. PROJECTILE VELOCITY DECAY IN THE FLUID -----	40
	D. PRESSURE VERSUS RADIUS AND TIME -----	49
V.	RECOMMENDATIONS -----	59
	COMPUTER PROGRAM -----	61
	LIST OF REFERENCES -----	67
	INITIAL DISTRIBUTION LIST -----	68
	FORM DD 1473 -----	69



## LIST OF FIGURES

1.	Ballistic Range Components -----	18
2.	Ballistic Range (Down-range View) -----	19
3.	Projectile Shapes -----	20
4.	Projectile Parameters -----	20
5.	Adjustable Time Delay Unit Circuitry -----	22
6.	Schematic of Shadowgraph Apparatus (Down-range View) -----	23
7.	Shadowbox, Tank and Stand Installation -----	25
8.	Front Wall Test Specimen, Pre-punched Hole -----	26
9.	Shadowgraphs After Projectile Impact Through a Pre-punched Front Wall -----	29
10.	Shock Radius vs. Time, $E_0 = 1600$ in-lb -----	32
11.	Shock Radius vs. Time, $E_0 = 7493$ in-lb -----	33
12.	Shock Radius vs. Time, $E_0 = 12323$ in-lb -----	34
13.	Shock Radius vs. Impact Energy, $E_0$ -----	35
14.	Solid Front Wall After Test -----	38
15.	Typical Damage to Solid Front Wall at Point of Impact -----	38
16.	Damage to Solid Front Wall (Mounted on Tank) -----	39
17.	Qualitative View of Projectile Energy and Velocity Decay in the Fluid -----	42
18.	Typical Deformation of Projectiles After Coming to Rest in the Fluid Filled Tank - Pre-punched Hole Results -----	44



19.	Projectile Distance in Fluid vs. Time, $E_0 = 1600$	
	in-lb -----	45
20.	Projectile Distance in Fluid vs. Time, $E_0 = 7493$	
	in-lb -----	46
21.	Projectile Distance in Fluid vs. Time, $E_0 = 12323$	
	in-lb -----	47
22.	Pressure vs. Radius from Impact - Complete Profile,	
	$E_0 = 1600$ in-lb -----	50
23.	Pressure vs. Radius from Impact, $E_0 = 1600$ in-lb --	51
24.	Pressure vs. Radius from Impact, $E_0 = 7493$ in-lb --	52
25.	Pressure vs. Radius from Impact, $E_0 = 12323$ in-lb -	53
26.	Pressure vs. Time for Three Radii, $E_0 = 1600$	
	in-lb -----	55
27.	Pressure vs. Time for Three Radii, $E_0 = 7493$	
	in-lb -----	56
28.	Pressure vs. Time for Three Radii, $E_0 = 12323$	
	in-lb -----	57



## LIST OF SYMBOLS

$A$	Area of deformed surface of the projectile
$B$	Constant in the equation of state; constant in velocity decay equation
$C_o$	Speed of sound in undisturbed fluid
$C_D$	Drag coefficient
$D$	Drag acting on projectile
$E_o$	Initial kinetic energy of the projectile; energy released at a point source
$\Delta E_s$	Change in projectile energy due to shock formation
$H$	Constant defined by equation (2.14)
$M_s$	Shock Mach number
$N$	Exponent defined by equation (2.14)
$P$	Pressure
$P_o$	Pressure in undisturbed fluid
$R_s$	Shock radius
$\dot{R}_s$	Shock velocity
$\ddot{R}_s$	Shock acceleration
$R_o$	Initial radius defined by equation (2.17)
$T$	Temperature
$V$	Projectile velocity
$V_o$	Projectile impact velocity
$\Delta V_s$	Change in projectile velocity due to shock formation
$e$	Specific internal energy of the fluid
$e_o$	Specific internal energy of undisturbed fluid
$e_1$	Specific internal energy after the shock





$f$	Non-dimensional pressure; equivalent flat plate area
$f_1$	Non-dimensional pressure after the shock
$g$	Non-dimensional internal energy
$g_0$	Non-dimensional internal energy of undisturbed fluid
$g_1$	Non-dimensional internal energy after the shock
$m$	Mass of projectile
$n$	Exponent defined in the equation of state
$q$	Exponent defined in density profile equation
$r$	Radius, radial coordinate
$s$	Specific entropy of fluid
$t$	Time
$u$	Particle velocity
$\bar{v}$	Specific volume ( $1/\rho$ )
$x$	Projectile distance traveled in tank
$\beta$	Shock decay coefficient
$\xi$	Non-dimensional radius
$\rho$	Density of the fluid
$\rho_0$	Density of the undisturbed fluid
$\rho_f$	Density of the fluid
$\phi$	Non-dimensional particle velocity
$\phi_1$	Non-dimensional particle velocity after the shock
$\psi$	Non-dimensional density
$\psi_1$	Non-dimensional density after the shock



## I. INTRODUCTION

Non-nuclear survivability of aircraft flying in a hostile arena has been studied throughout the history of aviation. Recent experiences in Vietnam have demonstrated the vulnerability of sophisticated aircraft to both small arms ground fire and the more complex surface-to-air defenses. Except for the rare case of a direct impact by a surface-to-air missile, the damage has been incurred by relatively small projectiles.

Tactical aircraft fuel tanks or cells have the largest surface area and volume of all vulnerable components. For this reason fuel cells have been most susceptible to damage. Projectile impact with fuel cells have caused fuel starvation, fire or explosion as well as extensive structural damage. The survivability of aircraft when a ballistic threat causes destruction of fuel filled tanks has been the main impetus behind this study. Astronomical costs of combat aircraft have made it cost effective to acquire more knowledge of the destructive mechanism to fuel cells. Another application of this information could be in space flight where meteoroid collisions are possible.

Projectiles which penetrate fluid filled cells cause damage many times more severe than that incurred by impact with an empty cell. With sufficient projectile energy there will be catastrophic failure of cell structural components. Hydraulic ram is the term used to describe such destructive



events. The hydraulic ram phenomenon is usually described by two phases: the shock phase and cavity phase. The effects of these phases are assumed to be sequential, occurring in the order listed above. Upon initial projectile impact, energy is transferred to the fluid, creating a strong hemispherical shock centered at the point of impact. The shock pressure loading may cause failure of the entrance wall. Pressures load the wall for a very short time because of geometrical attenuation. Essentially there is an impulsive load on the front wall during the shock phase.

As the projectile travels through the fluid, a cavity is formed. This phase has sometimes been called the bubble phase because of the bubble-like appearance of the cavity. Others have called this phase the drag phase, using the label to describe the mechanism which creates the cavity [Ref. 1]. Oscillation of the cavity volume produces pressure pulses that may be sufficiently intense to cause catastrophic failure of cell components. The intensity of the resulting pressure pulses is weaker than the shock phase pressure pulse but the duration is much longer [Ref. 2]. Ultimate destruction of tank components other than the entry wall has been generally attributed to the cavity phase.

Until recently, experimental data from studies of hydraulic ram have not been able to describe the basic phenomenon. Entire aircraft or wing sections have been destroyed while studying the phenomenon. This method of experimentation has become too costly; hence theory explaining the



phenomenon is necessary to defeat hydraulic ram. Much of the theory as it applies to hydraulic ram is still in its infancy. The complete mechanism is complex, requiring accurate and detailed analytical efforts. Correlation of theory with experiments must be accomplished simultaneously to assess theory validity.

Research at the Naval Postgraduate School has been designed to isolate and observe the individual aspects of hydraulic ram. The ballistic range has been used to study energy losses through aluminum plates, shock propagation and the cavity phase. Specific details were observed with the intent of applying the knowledge gained to the design of a survivable fuel cell.

This study has investigated the shock phase using the theory of Yurchovitch and Lundstrom [Refs. 1 and 2]. A computer program was formulated from the mathematical model. Experimental data for various projectile energies were compared with the results of the theory. Yurchovitch's formulation of shock radius as a function of time has agreed with the experimental data. These tests also have shown that damage to the tank front wall was not extensive enough for significant fuel leakage at the energy levels tested.







## II. ANALYTICAL STUDY

In order to predict the effects of the shock phase of hydraulic ram, it is necessary to study how the projectile impact energy affects the fluid that is disturbed. It was assumed that the impact energy,  $E_0$ , was known and was sufficient to create a strong hemispherical shock. The perturbation in the fluid can then be described by assuming that the shock radius is proportional to time to the 0.8 power, and that there is a power law density profile behind the shock. This formulation was suggested by Yurchovitch [Ref. 2]. Yurchovitch found that for a given fluid equation of state the energy transferred to the fluid determines the resulting flow field.

### A. SHOCK FRONT PRESSURES

The one-dimensional Rankine-Hugoniot equation for a shock moving through undisturbed fluid was used to determine shock front conditions. To complete the solution an equation of state was needed. The Tait Equation for isothermal compressibility of liquids,

$$-\frac{1}{\bar{v}} \left( \frac{\partial \bar{v}}{\partial p_s} \right) = \frac{1}{n[P+B(s)]} \quad , \quad (2.1)$$

where  $n$  is a constant for a specific liquid and  $B$  is a function of entropy only, was integrated along lines of constant pressure and entropy. Integrating equation (2.1) yields



$$P = B(s) \left[ \left( \frac{\bar{v}(T,0)}{\bar{v}(T,P)} \right)^n - 1 \right] \quad (2.2)$$

Assuming the changes across the shock are adiabatic and the pressure in the undisturbed fluid is small compared to the shock front pressure, B is given as

$$B = \frac{\rho_0 C_0^2}{n} \quad \text{where } C_0^2 = \left( \frac{dP}{d\rho} \right)_s \quad (2.3)$$

With the assumption that B and n are constant for a given fluid the equation of state is

$$P = \frac{\rho_0 C_0^2}{n} \left[ \left( \frac{\rho}{\rho_0} \right)^n - 1 \right] \quad (2.4)$$

For water n, a constant, was found to be 7.0 [Ref. 3].

Non-dimensionalization of the variables was found to be convenient and the following scheme was adopted:

$$\xi = \frac{r}{R_s(t)}$$

$$M_s = \dot{R}_s(t) / C_0$$

$$\psi(\xi, M_s) = \frac{\rho(r, t)}{\rho_0}$$

$$\phi(\xi, M_s) = \frac{u(r, t)}{\dot{R}_s(t)} \quad (2.5)$$

$$f(\xi, M_s) = \frac{P(r, t)}{\rho_0 \dot{R}_s^2(t)}$$

$$g(\xi, M_s) = \frac{e(r, t)}{\dot{R}_s^2(t)}$$



With the assumption that  $P_0 \ll P$  and  $e_0 \ll e$  the Rankine-Hugoniot equations become

$$\begin{aligned} 1 &= \psi_1 (1 - \phi_1) \\ f_1 &= \phi_1 \end{aligned} \quad (2.6)$$

$$g_1 = \frac{1}{2} f_1 \left( 1 - \frac{1}{\psi_1} \right)$$

and the equation of state is

$$f = \frac{1}{nM_S^2} (\psi^n - 1) \quad (2.7)$$

Solving the above equations for the parameters at the shock the following is obtained:

$$\psi_1 = \frac{1}{1 - \frac{1}{nM_S^2} (\psi_1^n - 1)} \quad (2.8)$$

$$\phi_1 = \frac{1}{nM_S^2} (\psi_1^n - 1) \quad (2.9)$$

$$f_1 = \phi_1 \quad (2.10)$$

By assuming values for  $\psi_1$ , the equation (2.8) can be solved for the shock Mach number,  $M_S$ . Subsequently,  $f_1$  and  $\phi_1$  versus  $M_S$  can be found. Conditions at the shock front are now known while conditions behind the shock front are still unknown.

#### B. PRESSURE FIELD BEHIND THE SHOCK

The density profile behind the shock is assumed to have the form

$$\psi = \psi_1 \xi^{q(M_S)} \quad (2.11)$$



To find  $q(M_S)$  the total mass enclosed by the shock,

$$\rho_0 R_S^3 2\pi \int_0^1 \psi \xi^2 d\xi ,$$

is equated to the original mass occupied by the enclosed volume,

$$2/3 \pi R_S^3 \rho_0$$

with the result

$$\int_0^1 \psi \xi^2 d\xi = 1/3 \quad (2.12)$$

Substituting the assumed density profile into (2.12),  $q(M_S)$  is found to be

$$q(M_S) = 3(\psi_1 - 1) \quad (2.13)$$

and the density function becomes

$$\psi = \psi_1 \xi^3 (\psi_1 - 1)$$

It is now possible to solve for the particle velocity,  $\phi$ , by substituting equation (2.12) into the one dimensional continuity equation and solving for the constant with  $\phi = \phi_1$ , at  $\xi = 1$  (the shock front location). The continuity equation is given by

$$(\phi - \xi) \frac{\partial \psi}{\partial \xi} + \psi \frac{\partial \phi}{\partial \xi} + 2 \frac{\phi \psi}{\xi} = -\beta M_S \frac{\partial \psi}{\partial M_S}$$

where  $\beta = R_S \ddot{R}_S / \dot{R}_S^2$  is the shock decay coefficient. With the above substitution and integration, the particle velocity profile is found to be

$$\phi = \phi_1 \xi$$





By substituting the density and particle velocity profiles into the momentum equation

$$(\phi - \xi) \frac{\partial \phi}{\partial \xi} + \beta \phi + \frac{1}{\psi} \frac{\partial f}{\partial \xi} = -\beta M_s \frac{\partial \phi}{\partial M_s}$$

and integrating, the pressure profile is found to be

$$f = f_1 + \frac{\psi_1}{q+2} (\xi^{q+2} - 1) \left[ \frac{\phi_1}{\psi_1} - \beta (\phi_1 + M_s \frac{\partial \phi_1}{\partial M_s}) \right]$$

where the constant of integration was solved with  $f=f_1$  at  $\xi=1$ .

The shock decay coefficient,  $\beta$ , can be found using the assumption that shock radius is given by

$$R_s = Ht^N \quad (2.14)$$

Experimental work done by NASA [Ref. 4] has found that

$$N = 0.8$$

for water. Substituting equation (2.14) into the expression for  $\beta$ , the decay coefficient becomes

$$\beta = -0.25$$

It is now possible to solve the pressure distribution function given the shock Mach number,  $M_s$ .

### C. SHOCK MACH NUMBER

By considering the initial energy being released at the center of symmetry in the fluid it is possible to equate the initial energy to the integral energy density behind the shock. The energy liberated initially,  $E_0$ , is distributed such that

$$E_0 = \int_0^{R_s} (e - e_0 + \frac{u^2}{2}) \rho 4\pi r^2 dr \quad (2.15)$$



Using the assumptions of a strong hemispherical shock as well as the density profile and particle velocity profile as derived previously, the integral equation (2.15) in non-dimensional form becomes

$$E_O = 2\pi\rho_O C_O^2 R_S^3 M_S^2 \int_0^1 \left[ \frac{1}{n M_S^2} (\psi_1^n - 1) \phi_1 + \phi_1^2 \xi^2 \right] \psi_1 \xi^{q+2} d\xi \quad (2.16)$$

The values of  $\rho_O$ ,  $C_O$  and  $n$  can be found for a given fluid. By choosing a Mach number the dependent variables  $\phi_1$  and  $\psi_1$  are known. Equation (2.16) can then be integrated and  $2E_O/R_S^3$  versus shock Mach number can be plotted. Given the energy released,  $E_O$ , it is then possible to find the shock Mach number as a function of shock radius from the plot of  $2E_O/R_S^3$  versus  $M_S$ .

There is however, an anomaly at a shock radius of zero. To avoid a finite amount of energy in zero volume or an infinite energy density, reference 5 suggests the initial radius be given as

$$R_O = \left( \frac{E_O}{\rho_O C_O^2 2\pi} \right)^{1/3} \quad (2.17)$$

Equation (2.17) was then used as the starting point for the solution of the theoretical pressures behind the shock.



### III. EXPERIMENTAL PROCEDURE

The basic components of the ballistic range used for this study are shown in figure 1. A down-range view of the ballistic range in figure 2 depicts the chronograph screen arrangement and test tank. The two spark sources above the tank were used as light sources for the shadowgraphs. Two rifles were used, a .22 caliber and a Remington .222 caliber. Commercial Remington .22 caliber Long Rifle ammunition was used. The .222 ammunition was hand loaded for testing so that the velocities of the projectiles could be adjusted and would be known more precisely. Sierra bullets classified as spitzers were used. Figure 3 displays the corresponding shapes of the projectiles. The mass of the .222 caliber and .22 caliber projectiles are listed in figure 4 along with the parameters used to calculate the energy of each configuration. The area and drag coefficient parameters listed in figure 4 were experimental values used to calculate the velocity decay that was experienced during projectile passage through the test tank.

AVTRON, No. A914T333, chronograph screens were used to provide start and stop pulses to Monsanto 101 B counters. As the projectile passed through the screen the pulse circuit was energized. The first screen started the first counter and the second screen stopped the first counter and simultaneously initiated the second counter. The third screen stopped the second counter. The projectile impact velocity was computed using these times and distance measurements.



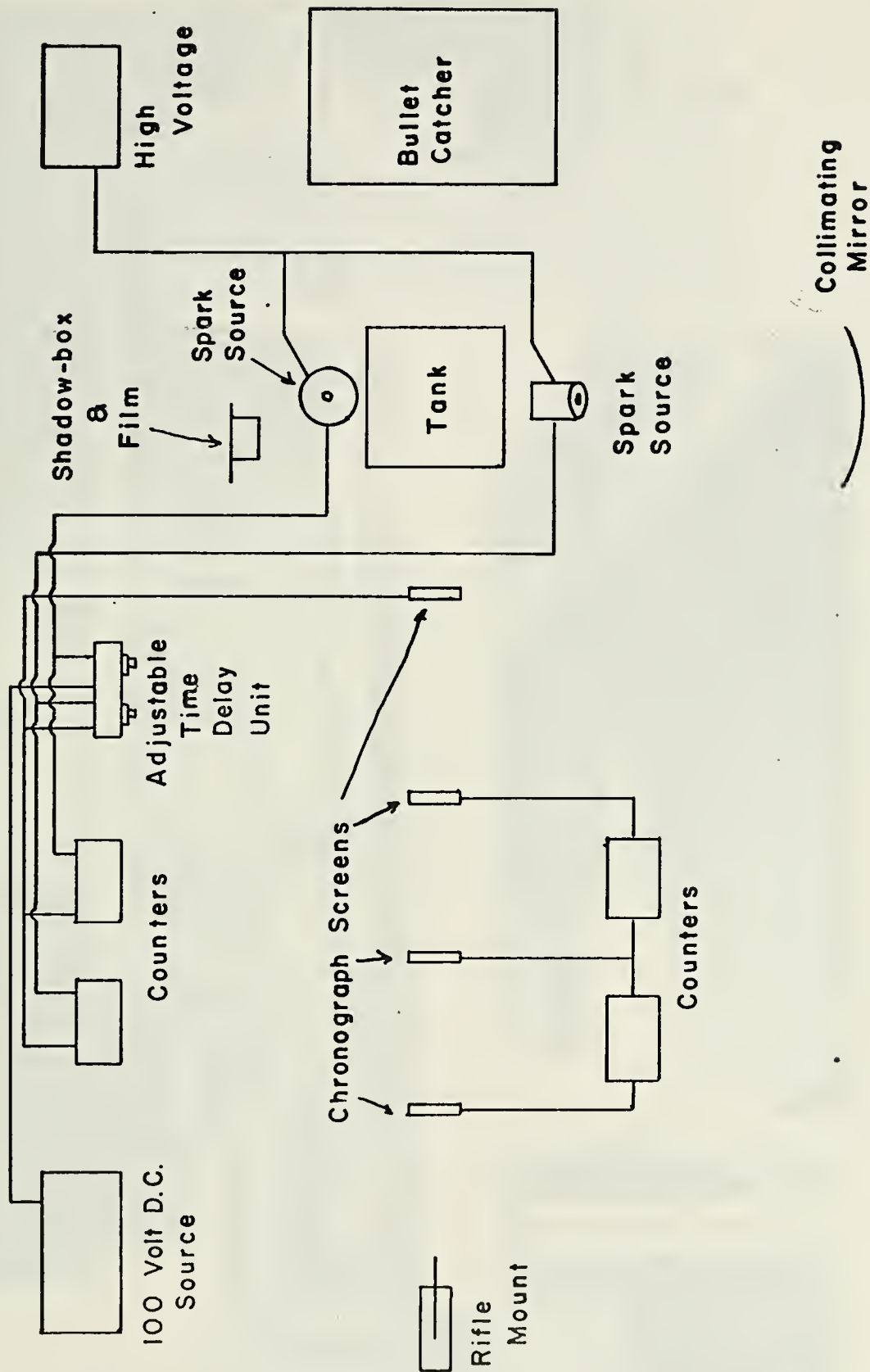


Figure 1. Ballistic Range Components





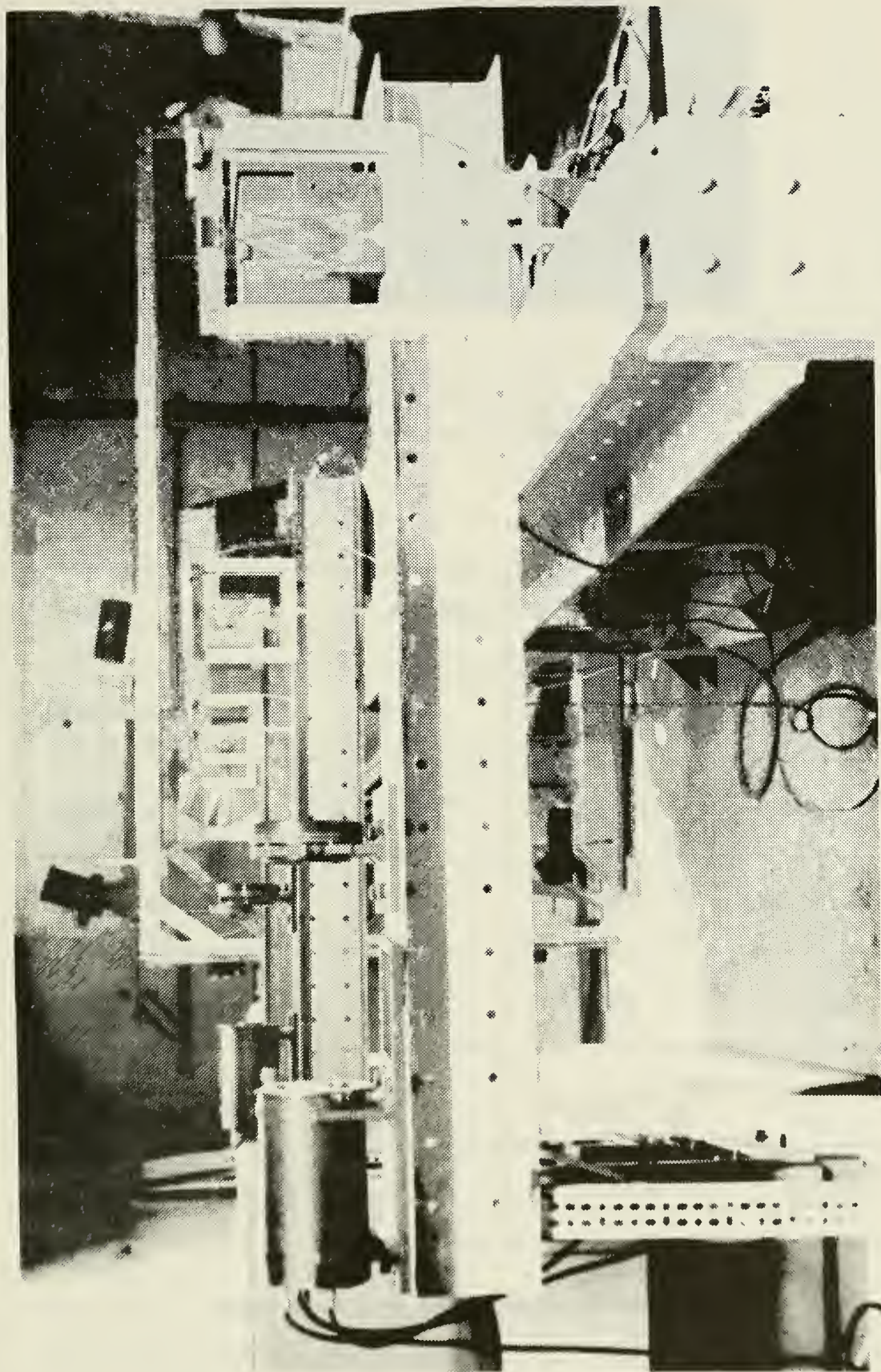


Figure 2. Ballistic Range (Down-range View)



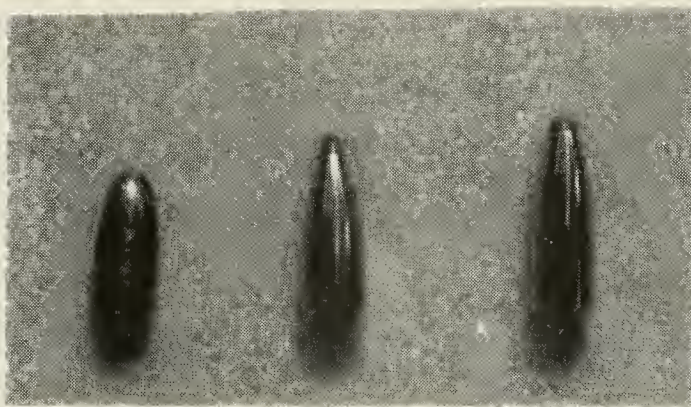


Figure 3. Projectile Shapes (L. to R.: .22 caliber,  $m=5.75 \times 10^{-3}$  lb, .222 caliber,  $m=6.43 \times 10^{-3}$  lb, .222 caliber,  $m=7.85 \times 10^{-3}$  lb)

Caliber	.22 Long Rifle	.222 Remington	.222 Remington
Impact Velocity, $V_0$ (ft/sec)	1200	2500	2900
Projectile Mass, $m$ (lb <sub>m</sub> )	$5.75 \times 10^{-3}$	$6.43 \times 10^{-3}$	$7.85 \times 10^{-3}$
Impact Energy, $E_0$ (in-lb)	1600	7493	12323
Experimental Drag Coefficient, $C_D$	1.20	0.45	0.50
Frontal Area of Projectile After Traversing Fluid, $A$ (in <sup>2</sup> )	0.122	0.098	0.165
Equivalent Flat Plate Area, $f (=C_D A)$ (in <sup>2</sup> )	0.146	0.044	0.083

Figure 4. Projectile Parameters





The events within the fuel cell were timed with two additional counters. A fourth chronograph screen provided a signal pulse which was distributed to the adjustable time delay unit (ATDU) and the two remaining counters to initiate them. The main element of the adjustable time delay unit circuitry was a Signetic, N74123, retriggerable, monostable multivibrator as shown in figure 5. Within the ATDU were two duplicate delay circuits to provide a 100 volt output pulse to each spark source. The time delay for both circuits in the unit was adjustable; however, the duplicate circuit delay was initiated by the first circuit's output. This resulted in the delay time for the second output pulse from the ATDU being the sum of the delay time of the first circuit plus the delay of the second circuit. The delay time range for the first circuit was 500 to 1600 micro-seconds, while the second circuit provided an additional delay of 5 to 15 micro-seconds. The 100 volt output pulses going to the spark sources were also used to stop the two counters. The first output pulse went to the spark source providing illumination for a shadowgraph in the horizontal plane, while the second pulse triggered the spark source for a shadowgraph in the vertical plane. Each counter therefore measured the time the shadowgraphs were taken.

Two 16-inch collimating mirrors were used to pass light through the tank. The spark sources were located at the focal point of their respective mirrors. Figure 6 demonstrates the arrangement of the tank with respect to the



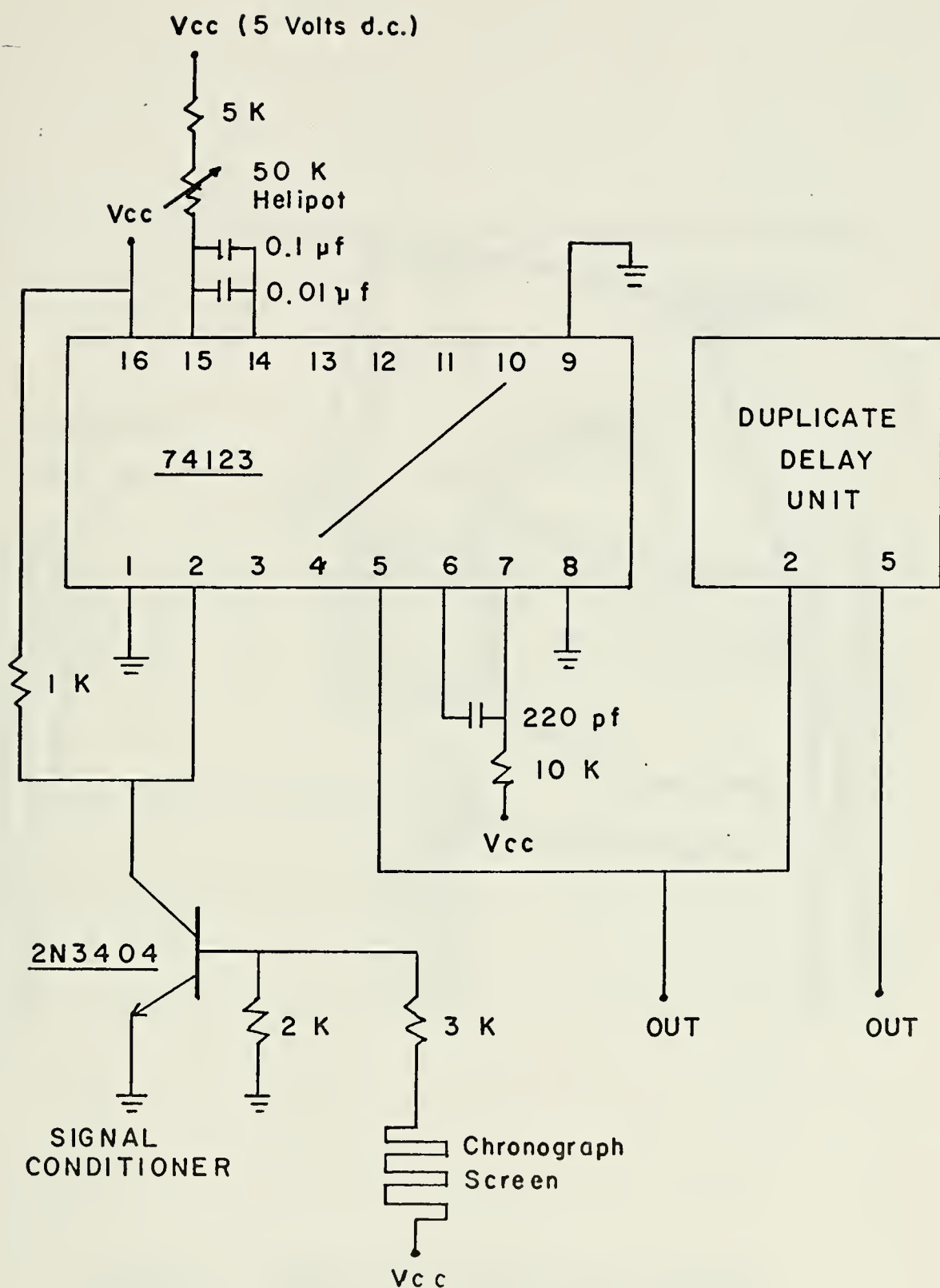


Figure 5. Adjustable Time Delay Unit Circuitry





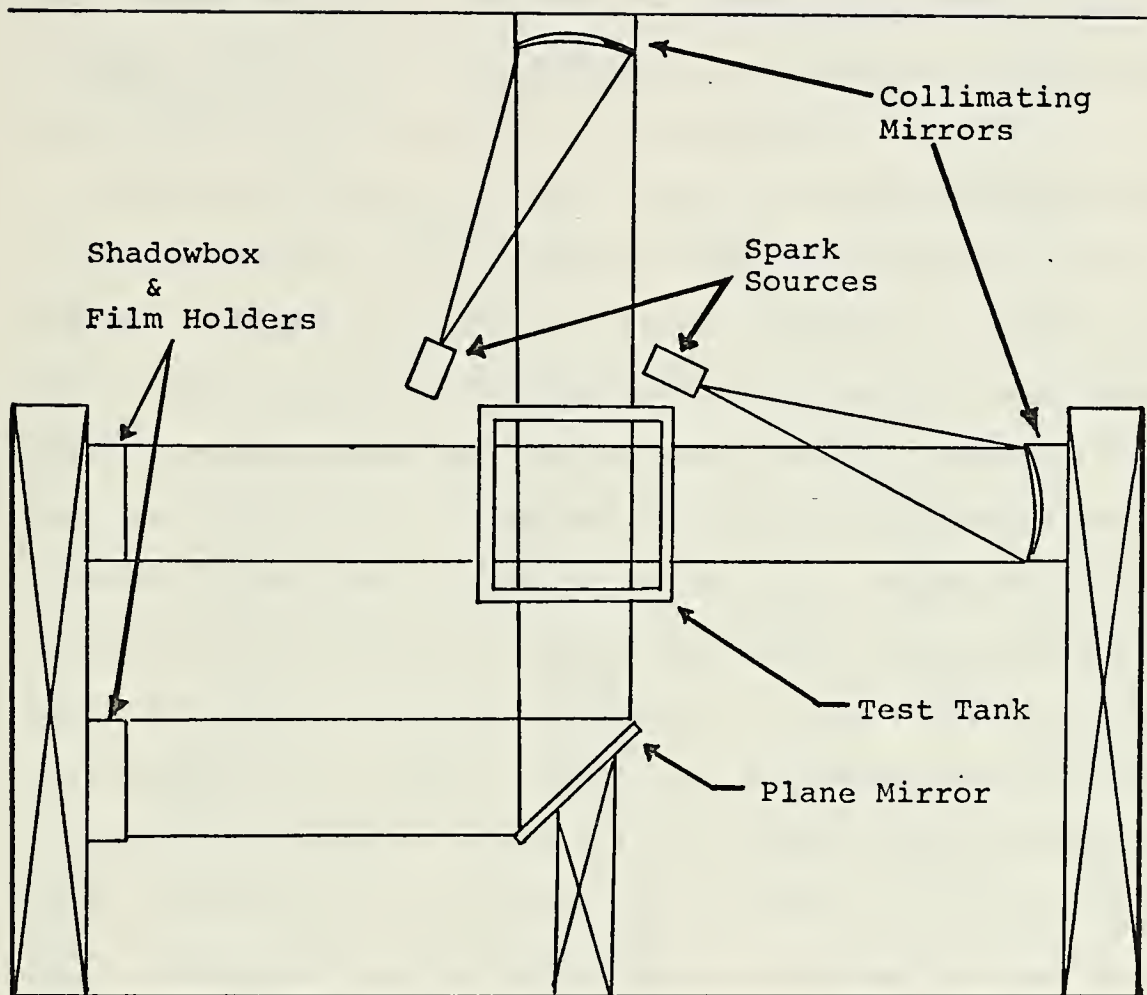


Figure 6. Schematic of Shadowgraph Apparatus  
(Down-range View)



spark sources, mirrors and photographic plates. The side and bottom walls of the tank were made of plexiglass through which very little light attenuation occurred. One side wall and the bottom wall had grid lines etched in the plexiglass for use in measuring the shock radius and cavity distance. High speed Polaroid film, Type 57, was used for the shadow-graphs. A ground, first surface mirror was used to deflect the light in the vertical plane 90 degrees.

The tank or test cell had front wall inner dimensions of 17.5 inches wide and 17.0 inches high with a depth of 17.0 inches. Figure 7 contains a view of the tank. The main member of the front wall was one-inch thick aluminum and served as a mounting plate for the specimens used to simulate fuel cell wall material. To accommodate the test material the mounting plate had a circular cut-out 15.0 inches in diameter. The specimen was mounted behind the mounting plate with 16 bolts arranged in a circular pattern. A front wall of 7075-T6 Aluminum, .090 inches thick, with a prepunched entry hole is shown in figure 8. This wall was used in the experiments with the exception of the few tests which used a solid front wall. The rear wall of the tank was identical to the front wall.

To provide support for the front and rear walls aluminum angle strips were placed longitudinally at the four corners of the tank. The angle strips were bolted to the front and rear mounting plates. In addition to providing structural





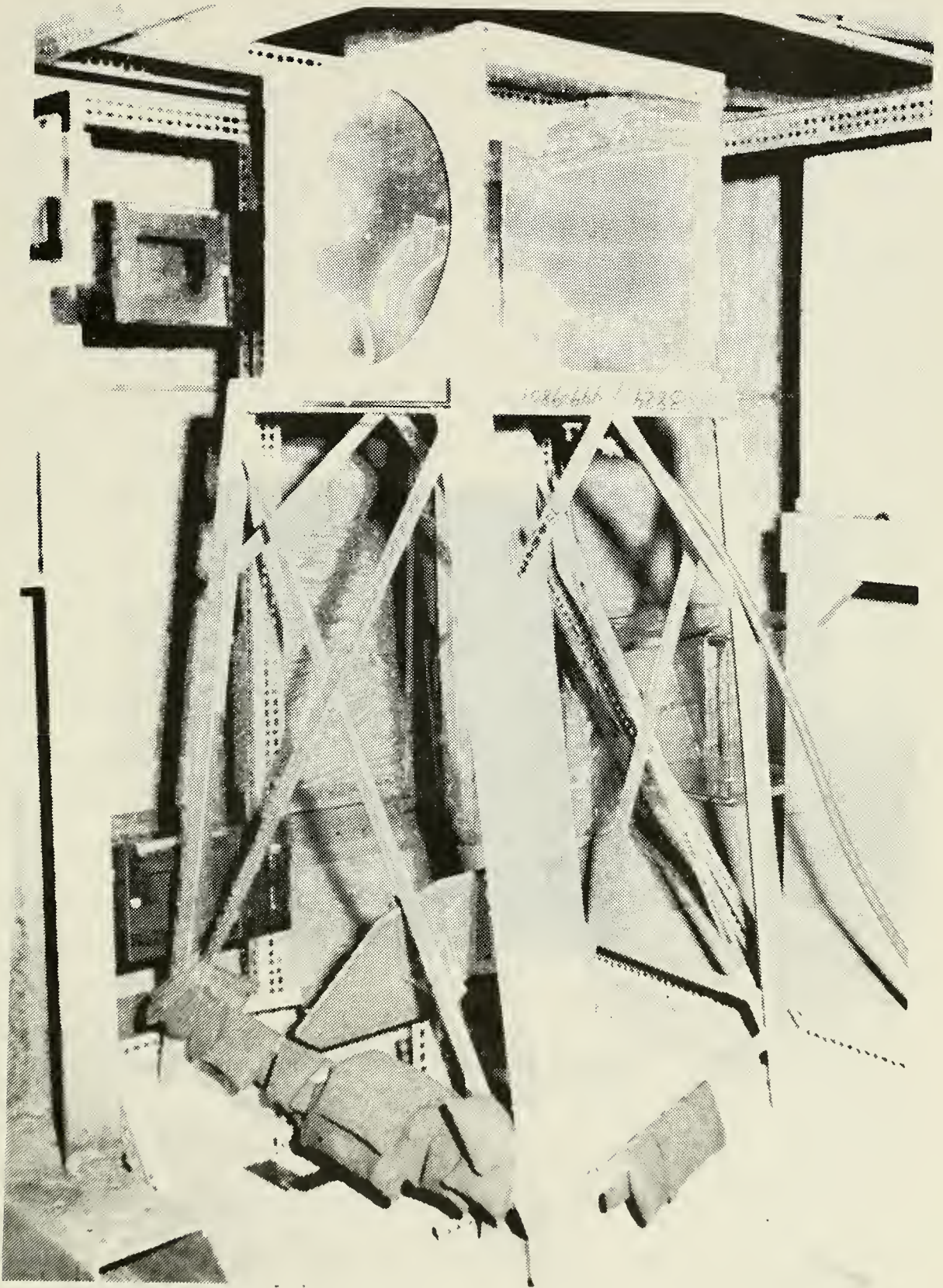


Figure 7. Shadowbox, Tank and Stand Installation



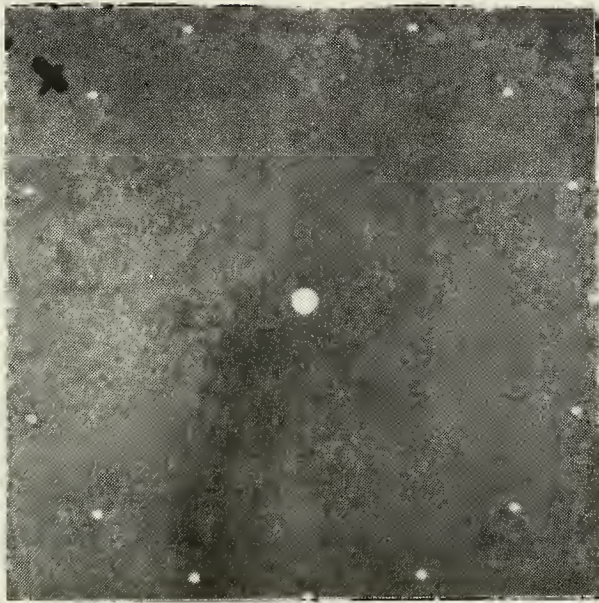


Figure 8. Front Wall Test Specimen,  
Pre-punched Hole





rigidity, the angle strips retained the one-inch thick plexiglass tank walls. The top of the tank was open.

Room Temperature Vulcanizing (RTV) rubber sealant was used at all joints to make the tank water tight. At the two highest energy levels the sealant around the front wall had to be replaced several times. Apparently the shock pressures were sufficient to deteriorate the sealant bond to the plexiglass and aluminum. Tape was used to prevent water spillage through the prepunched hole and to avoid any significant energy loss during penetration.

During initial testing the tank was set on the top of the stand. It was discovered that although the tank was restrained by the stand in longitudinal and lateral motion, angular tank movement was created by the moment arm and the force of impact at the center of the tank. This invalidated the shock radius data and the tank was subsequently bolted to the frame. It was also discovered that the tank and stand would move approximately eight inches during a test firing. To alleviate this problem the front two legs of the stand were bolted to the floor. Eventually these bolts worked loose and finally all four legs were bolted to the floor and 150 pounds of sandbags were placed on the stand.

The experiment was run at three energy levels. One energy level was tested before continuing with the next higher energy level. By varying the time delay with the ATDU, shadowgraphs of the shock radius versus time were taken. It was also possible to measure the projectile distance into

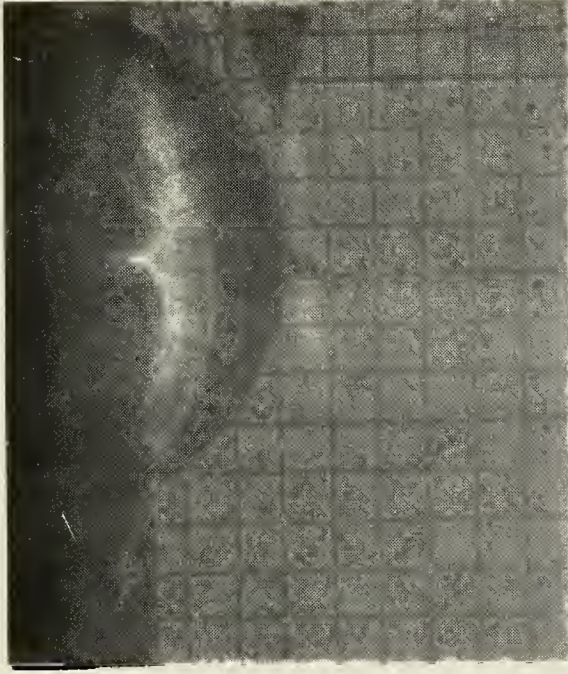


the tank versus time. Figure 9 shows a pair of typical shadowgraphs. The impact velocity of the projectile was computed from the times on the first two counters and the distance between chronograph screens. The shadowgraph times were measured by the third and fourth counters.

Acquiring data for the .22 caliber was found to be very difficult because of the deviation in impact velocities from one test firing to another. A good estimation of velocity was required prior to a test to compute projectile time of flight from the fourth chronograph screen to the tank wall. That time plus the desired time for photographing the shock radius determined the delay time used to set the adjustable time delay circuit. Since the .222 caliber projectiles were hand loaded, the impact velocities were more predictable. However, in the .222 caliber tests the velocity had a sufficient deviation to make it difficult to shadowgraph a shock radius smaller than one inch.

The data were reduced by first calculating the projectile impact velocity. The time of flight of the projectile from the fourth chronograph screen to the tank was then calculated. This time was subtracted from the elapsed time of the shadowgraphs as measured by the third and fourth counters. The result was the time corresponding to the shock position from initial impact at the front wall. Shock radius, measured on the shadowgraph, was then plotted at the corresponding time. Measurements of the shock radius were accurate to  $\pm 0.02$  inches.





$t = 1 \mu\text{sec}$



$t = 24 \mu\text{sec}$

Figure 9. Shadowgraphs After Projectile Impact Through  
a Pre-punched Front Wall





Projectile distance into the tank versus time data were also accumulated. The shadowgraph at 24 micro-seconds in figure 9 shows that the projectile was not distinctly visible. Work done by McMillen [Ref. 6] implies that the projectile nose is at the tip of the light cusp seen at the leading edge of the cavity shadow. Light refraction caused by density gradients in the flow field forms this nearly triangular region called the cusp.





#### IV. RESULTS AND CONCLUSIONS

This research was conducted to verify the theoretical prediction of shock radius as a function of time. In all but four cases, the data collected utilized projectiles impacting the fluid through a pre-punched hole in the front wall of the tank. There were four data points taken where the projectile passed through a solid front wall before coming in contact with the fluid. This was done at the conclusion of the experiment to see if there was a departure from the trends of the previous data and to obtain a qualitative estimate of the extent of shock phase damage. The solid front wall data were taken using the highest energy level tested (12323 in-lb).

##### A. SHOCK RADIUS VERSUS TIME - PRE-PUNCHED FRONT WALL

Figures 10, 11, and 12 show the experimental data and the theoretical prediction of shock radius versus time. Seldom were projectile velocities prior to impact constant during the testing. Changes in velocity have a direct influence on the initial energy. The data were plotted and compared, however, assuming constant impact energies. It was therefore necessary to determine the shock radius sensitivity to changes in energy. A plot, using theoretical predictions of the shock radius versus impact energy for a constant time (figure 13), indicates that there is an insignificant change in shock radius for typical experimental



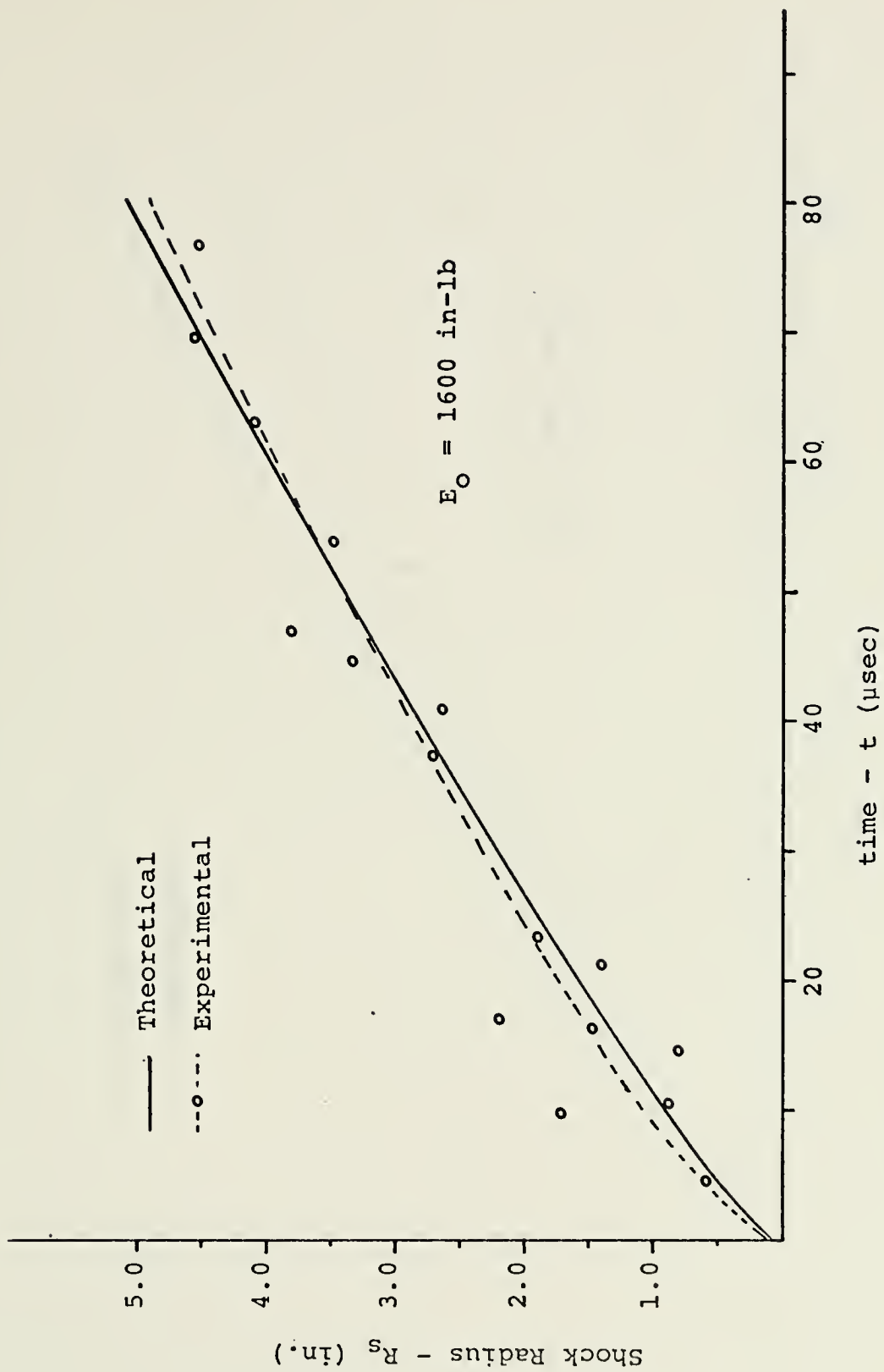


Figure 10. Shock Radius vs. Time,  $E_0 = 1600 \text{ in-lb}$



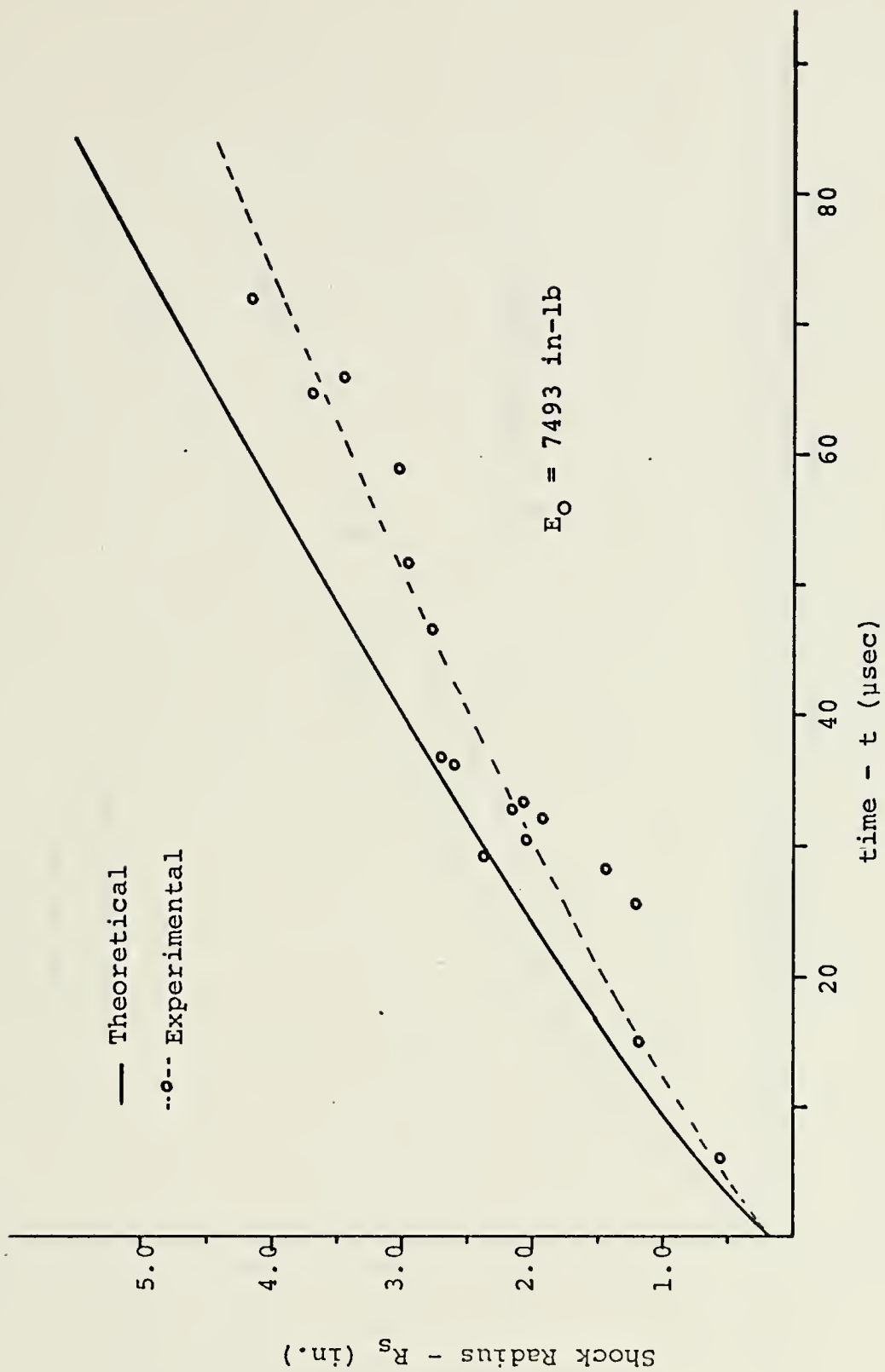


Figure 11. Shock Radius vs. Time,  $E_0 = 7493$  in-lb



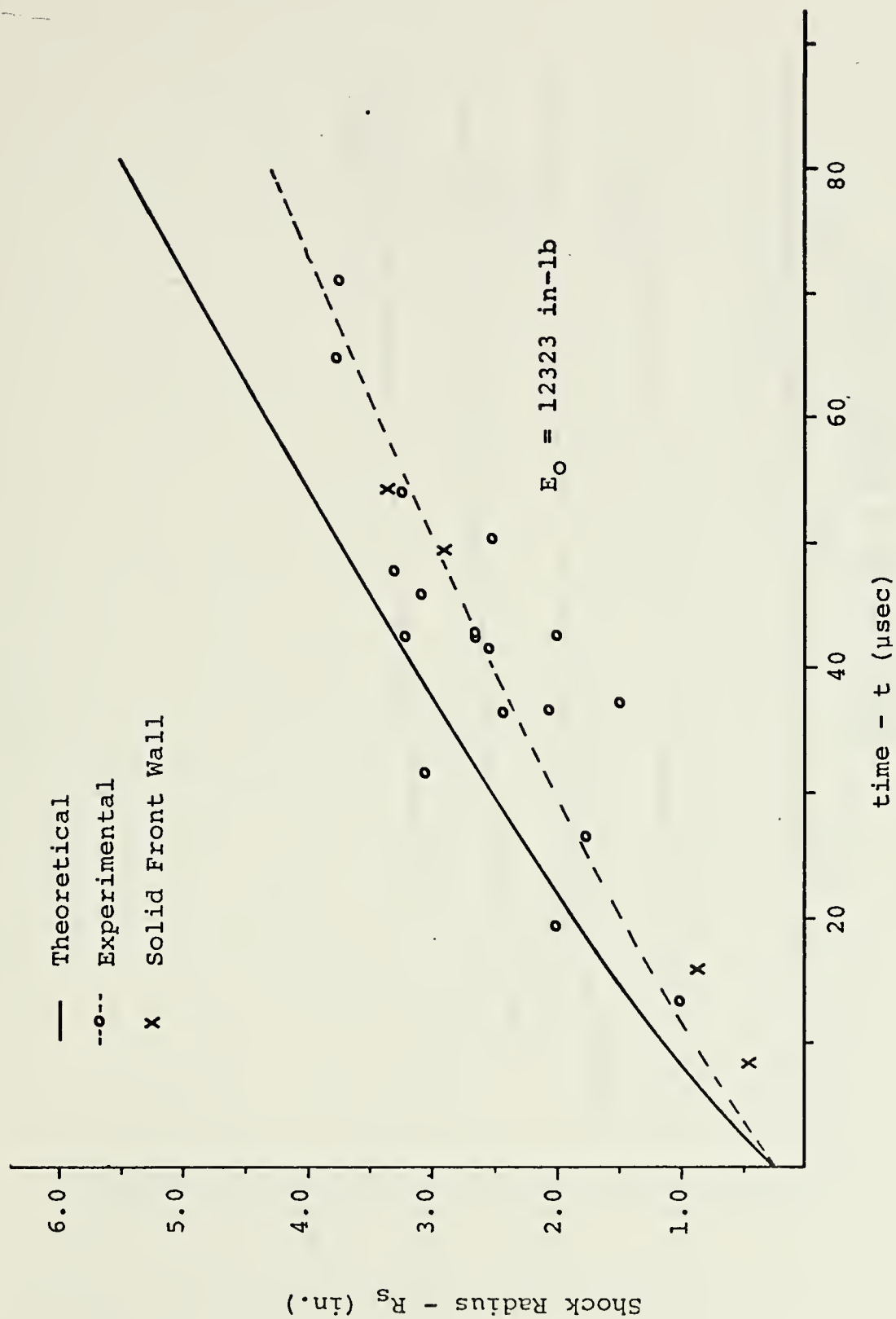


Figure 12. Shock Radius vs. Time,  $E_0 = 12323 \text{ in-lb}$





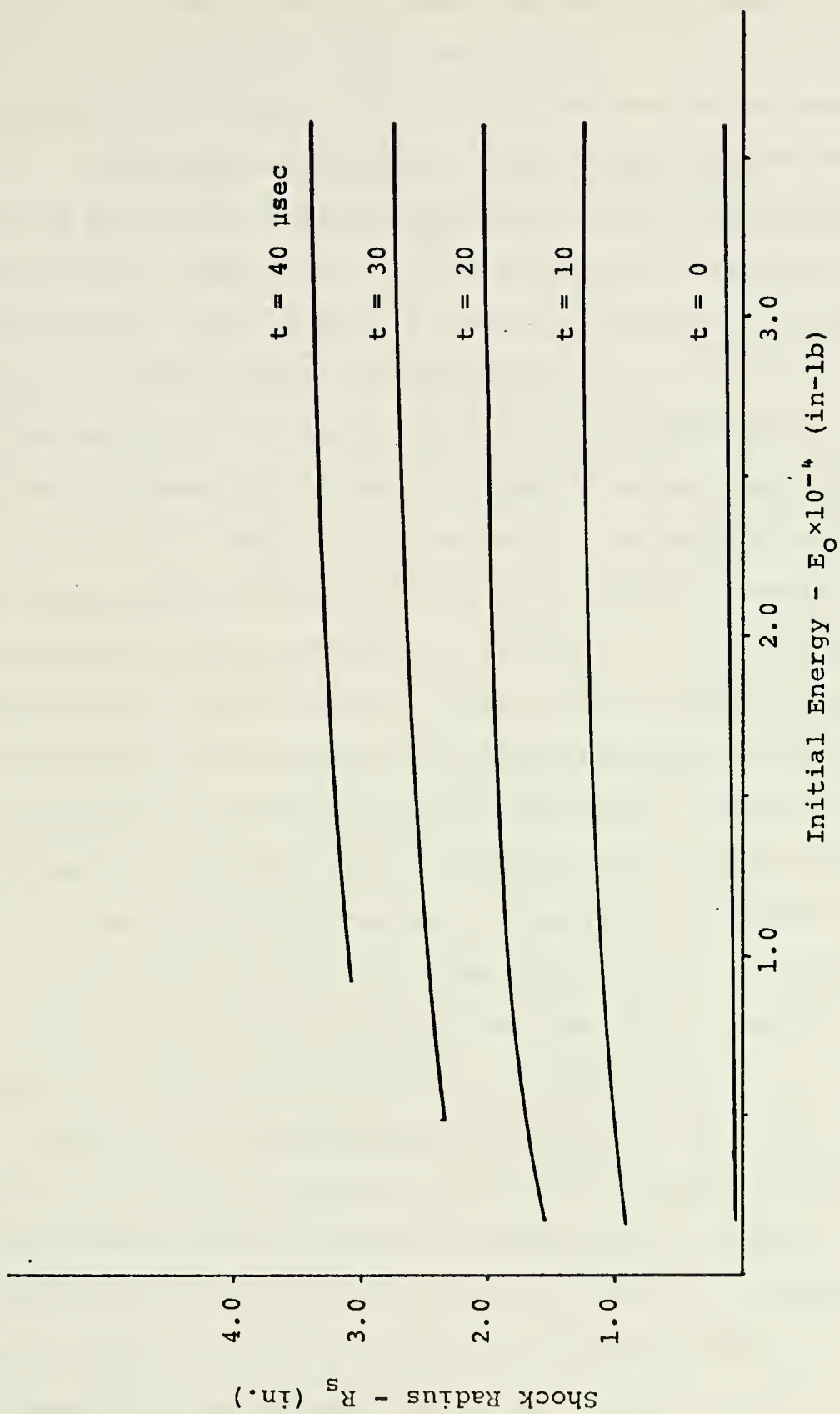


Figure 13. Shock Radius vs. Impact Energy,  $E_0$



variations of impact energy about the reference energy. The impact energy calculated from experimental data of the individual tests was within  $\pm 200$  in-lb of the comparison energy level. Corresponding changes in shock radius were of an order of magnitude smaller than the accuracy of the radius measurements. Therefore, no corrections were applied to the measured shock radii for experimental differences in impact energy about the comparison energy level.

The data for an initial impact energy of 1600 in-lb had the best agreement with theory. Theory assumes that the total projectile energy is deposited at the point of impact. The shadowgraphs indicate, however, that none of the projectiles came to rest at the point of impact. At the higher energy levels (7493 in-lb and 12323 in-lb) the data fell below the theoretical results which implies generation of weaker shocks than those predicted by theory. This may be explained by considering the projectile as a piston in the early stages of shock formation. It would be expected that the rate of change of fluid volume displaced by the piston determines the momentum exchange between the projectile and fluid, hence the shock strength. The shape of the .22 caliber projectile is noticeably more blunt than the .222 caliber projectiles (see figure 2). This means that the .22 caliber projectile would have a greater rate of change of fluid volume displaced in the formation stage of the shock phase. This would produce conditions which are more closely represented by the assumptions of the theory. It is expected



that blunt projectiles or warhead fragments produce shocks that agree closely with the theory.

Eventually the shock becomes acoustic because of geometrical attenuation. The theoretical predictions for the time at which the shock is acoustic were 22 micro-seconds at 1.71 inches for the energy level of 1600 in-lb, 36 micro-seconds at 2.81 inches for the energy level of 7493 in-lb and 44 micro-seconds at 5.40 inches for the energy level of 12323 in-lb. Theory assumed no counterpressure ( $P_0 \ll P$ ). For this reason it is expected that the shock will actually become acoustic earlier than theory predicts. The experimental results for this study exhibited too much scatter to accurately determine when the shock becomes acoustic. It is reasonable to assume the duration of the shock phase is accurate in order of magnitude. The cavity begins to oscillate at a time on the order of 1000 micro-seconds, which implies a distinct time separation between the shock and cavity phases. This research has shown that the shock phase and cavity phase may be studied independently.

#### B. SHOCK RADIUS VERSUS TIME - SOLID FRONT WALL

The four data points taken for the case of a projectile passing through a solid front wall and then into the fluid are shown in figure 12 as X symbols. Time limitations prevented the collection of more data. The limited results do not indicate a significant departure from the pre-punched data. Figures 14, 15 and 16 show typical damage to the .043 inch thick, 6061-T6 Aluminum front wall specimen. The front





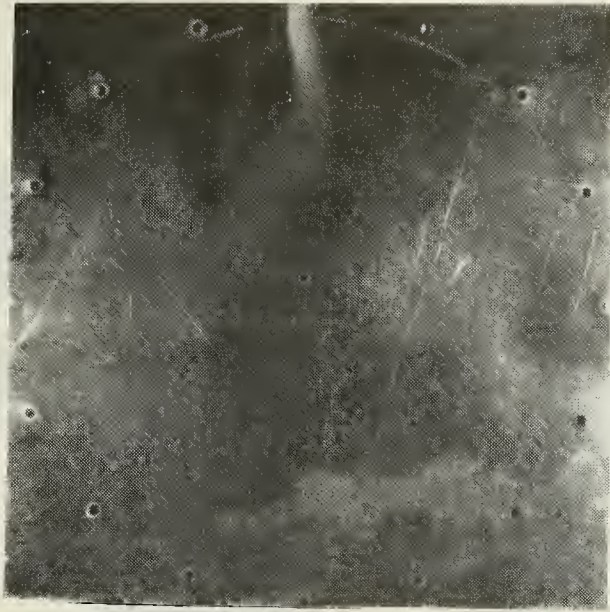


Figure 14. Solid Front Wall After Test (6061-T6 Aluminum, .043 in. thick,  $E_0 = 12323$  in-lb)

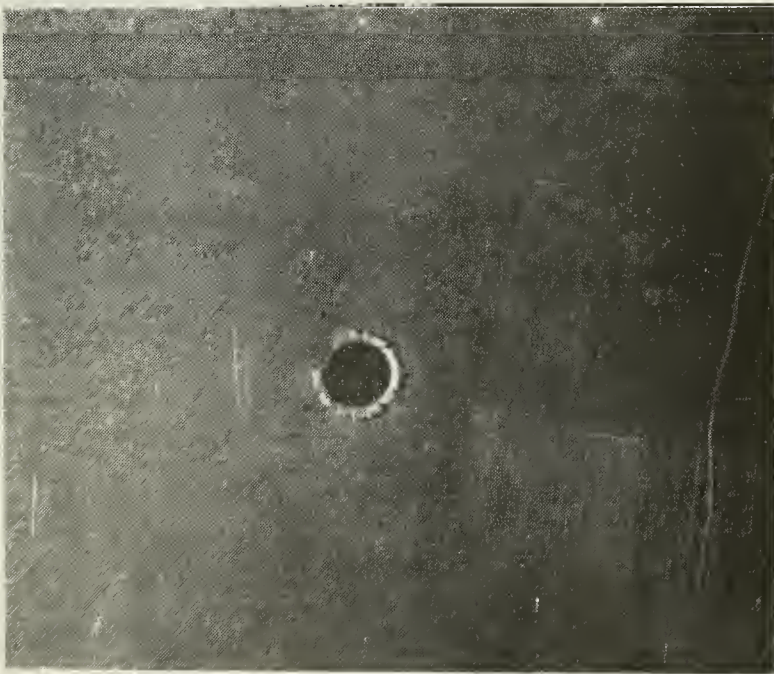


Figure 15. Typical Damage to Solid Front Wall at Point of Impact (Front view, 6061-T6 Aluminum, .043 thick,  $E_0 = 12323$  in-lb)





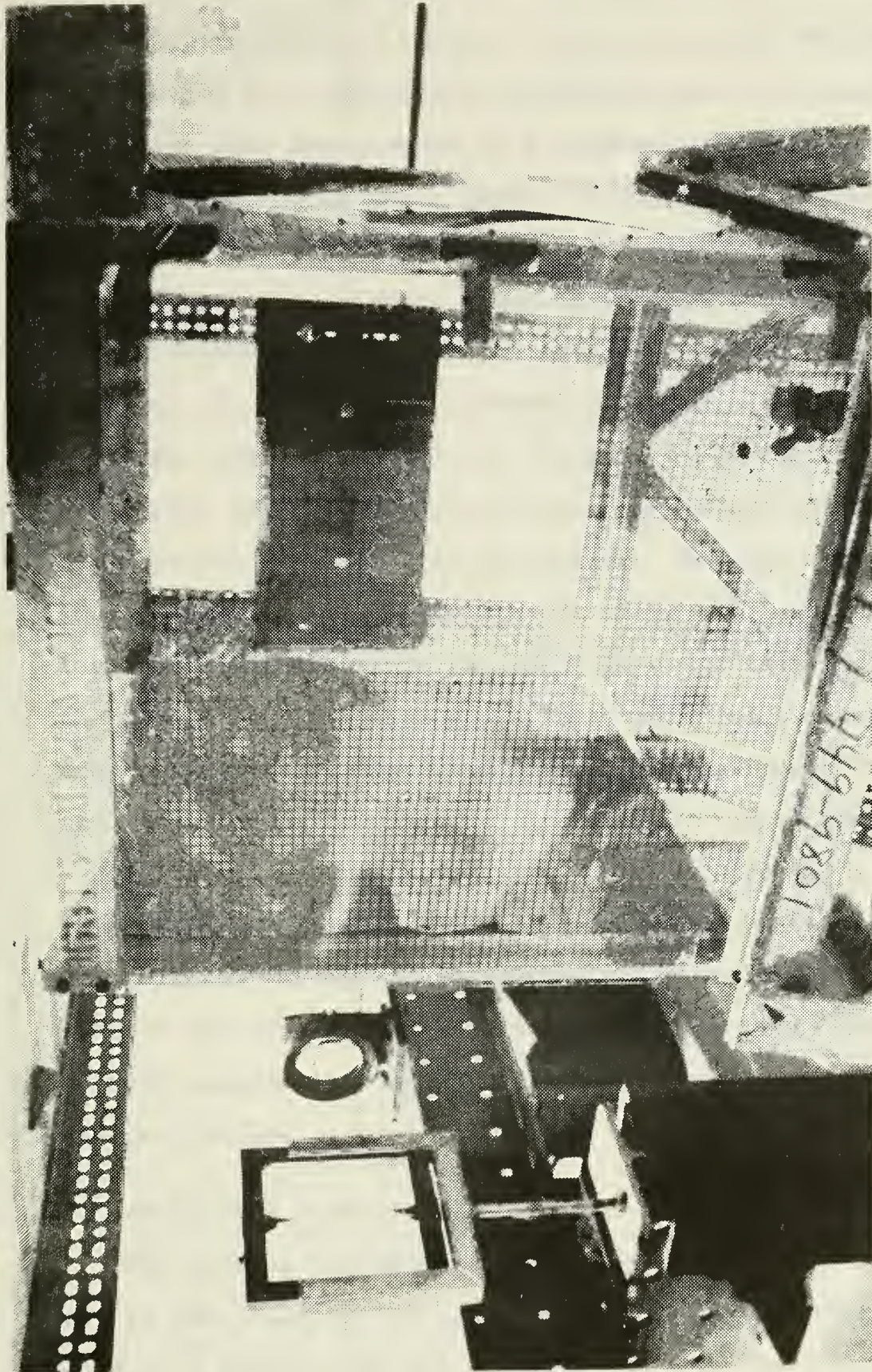


Figure 16. Damage to Solid Front Wall (Mounted on Tank)





wall experienced plastic deformation, became concave in the outward direction and buckled. There was some additional deformation at a few of the restraining bolt locations believed to have been caused by a slightly unsymmetrical load distribution. This was a result of projectile impact not being at the true center of the front wall. Projectile penetration caused no visible signs of cracking; although there was permanent deformation, the pressure load on the front wall was not sufficiently severe to produce cracking.

Soper [Ref. 7] calculated the percent energy change versus impact velocity for penetration of various thickness aluminum plates with no fluid foundation. For the specimen and impact velocity used in this study there was just under a 10% loss of energy predicted in penetrating the front wall. Using the theoretical prediction of shock radius versus impact energy in figure 13, there would be an insignificant change in the shock radius for such a 10% change of impact energy.

The shape of the projectiles after penetrating a solid front wall was significantly different than the projectiles which passed through a pre-punched hole. This was the result of the copper jacket on the projectile being deformed by both penetration and the stagnation pressure loading on the projectile.

#### C. PROJECTILE VELOCITY DECAY IN THE FLUID

The impetus for investigating the projectile velocity decay in the fluid is the requirement to know the time rate of change of energy exchange in order to study the cavity phase



[Ref. 1]. It is difficult to predict velocity decay because of the many dependent variables of the problem. The analysis of velocity decay suggested by Lundstrom [Ref. 1] was utilized. The equation of motion used was

$$D = -m \frac{dV}{dt} = \frac{1}{2} \rho_f V^2 C_D A \quad (4.1)$$

Assuming a constant deformed projectile area, constant drag coefficient and constant projectile mass it was possible to rearrange equation (4.1) and integrate, which yields

$$\frac{V}{V_0} = e^{-(\rho_f C_D A / 2m) x} \quad (4.2)$$

Further rearranging and integration from initial conditions of  $x=0$  at  $t=0$  yields the following expression for projectile position as a function of time

$$x = \frac{1}{B} \ln(BV_0 t + 1) \quad (4.3)$$

where

$$B = \frac{\rho_f C_D A}{2m}$$

The density for the undisturbed fluid,  $H_2O$ , was assumed constant. In calculating the theoretical results of equation (4.3) the value used for  $V_0$  was the projectile velocity immediately prior to impact with the fluid. It may be more suitable to use the velocity of the projectile at the completion of shock generation phase as the initial velocity in the fluid,  $V_0$ . Figure 17 is provided to point out a possible discontinuity of the projectile energy and velocity profile





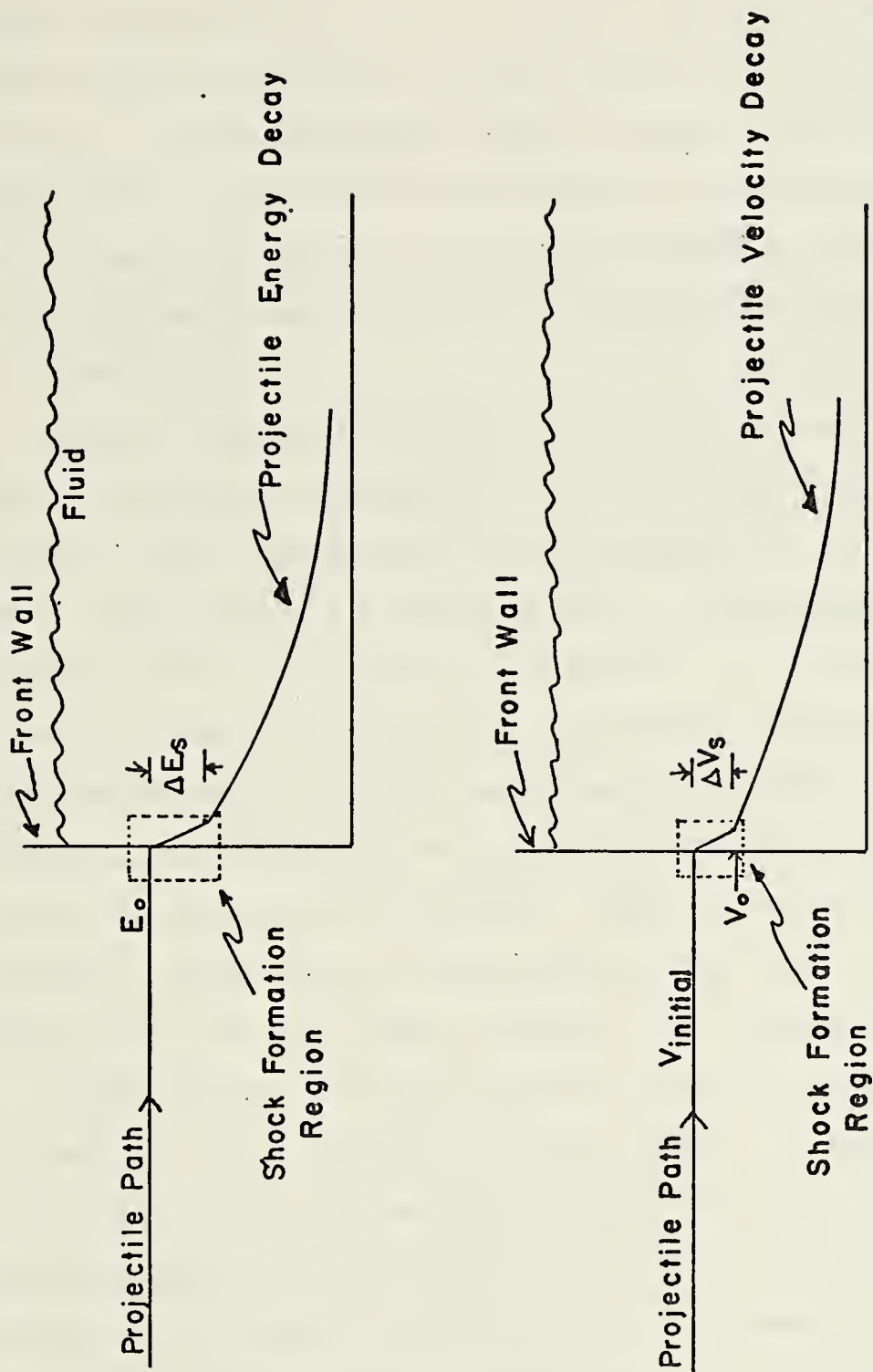


Figure 17. Qualitative View of Projectile Energy and Velocity Decay in the Fluid



during shock formation. The initial location and time of this event would still be adequately described by  $x=0$  and  $t=0$ . A value for the change in projectile energy due to shock formation,  $\Delta E_s$ , or the change in projectile velocity due to shock formation,  $\Delta V_s$ , would make it possible to solve for  $V_0$ . If the experimental data had less scatter than in this study it would have been possible to determine the value of  $\Delta E_s$  required for the theoretical results to be coincident with such experimental results. It would then be possible to solve for  $V_0$ .

Typical projectile shapes after coming to rest in the fluid are shown in figure 18 for each energy level tested. Figure 4 shows the values for the average final deformed area, drag coefficient and mass used to calculate the theoretical curves in figures 19, 20 and 21. Holm [Ref. 8] has shown that the projectiles possess dynamic stability and do not tumble, which contributes to the deformation experienced. Stagnation pressures on the order of  $10^4$  psi were found to exist on the projectile surface. These pressures are large enough to cause plastic deformation of the lead .22 caliber projectiles and the copper jacketed, .222 caliber projectiles.

Approximately fifty-one percent (51%) of the .22 caliber projectile impact velocity was lost within 1.5 inches of the front wall. The .222 caliber projectiles with an initial impact energy of 7493 in-lb only lost 17% of their impact velocity at 1.5 inches. Projectiles with an energy 12323 in-lb lost 25% at the same penetration depth. Percentage differences of the energy lost at the same distance from impact





Figure 18. Typical Deformation of Projectiles After Coming to Rest in the Fluid Filled Tank - Pre-punched Hole Results (L. to R.: .22 caliber,  $E_o = 1600$  in-lb; .222 caliber,  $E_o = 7493$  in-lb; .222 caliber,  $E_o = 12323$  in-lb)



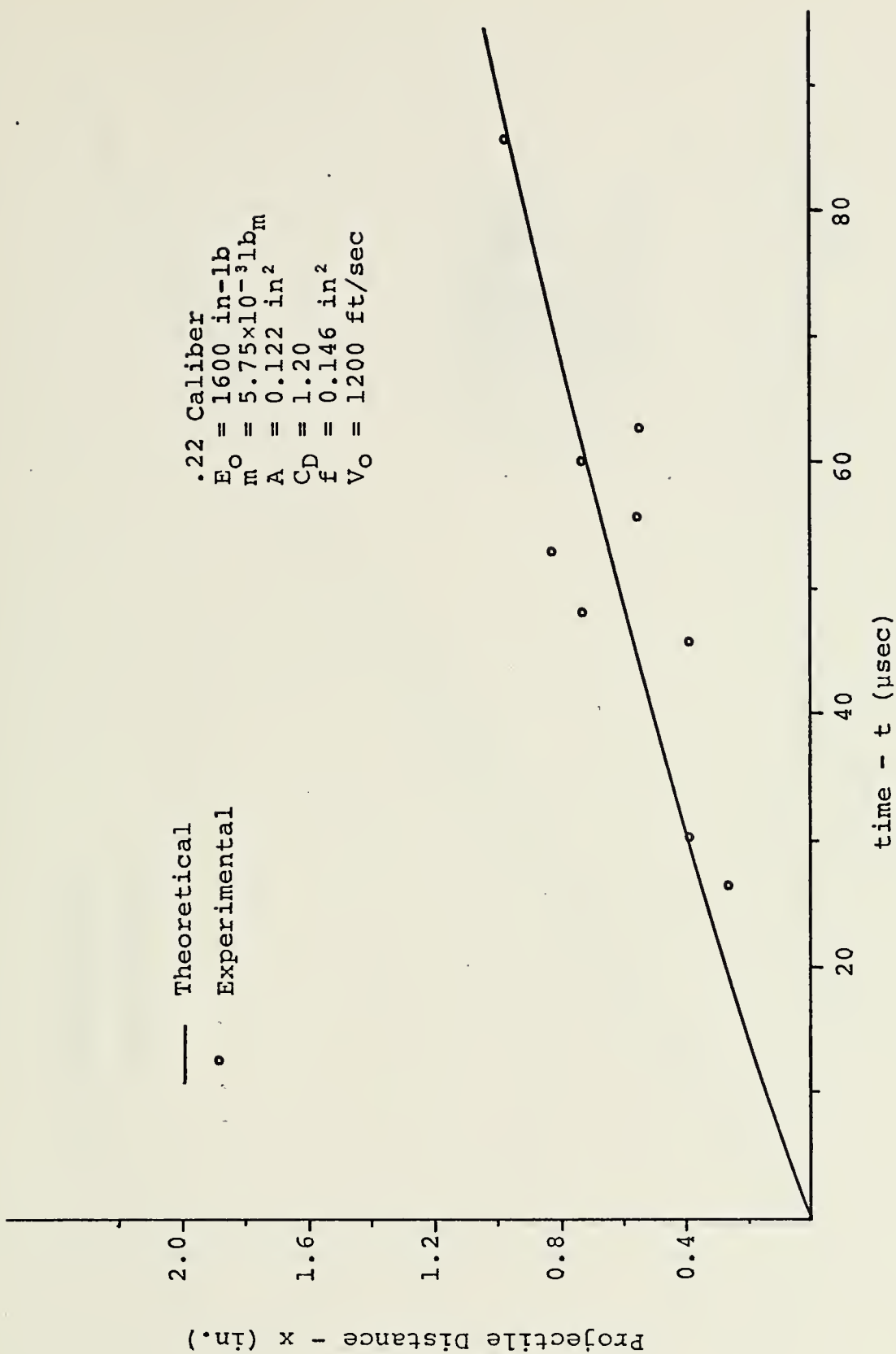


Figure 19. Projectile Distance Traveled in Fluid vs. Time,  $E_0 = 1600 \text{ in-lb}$





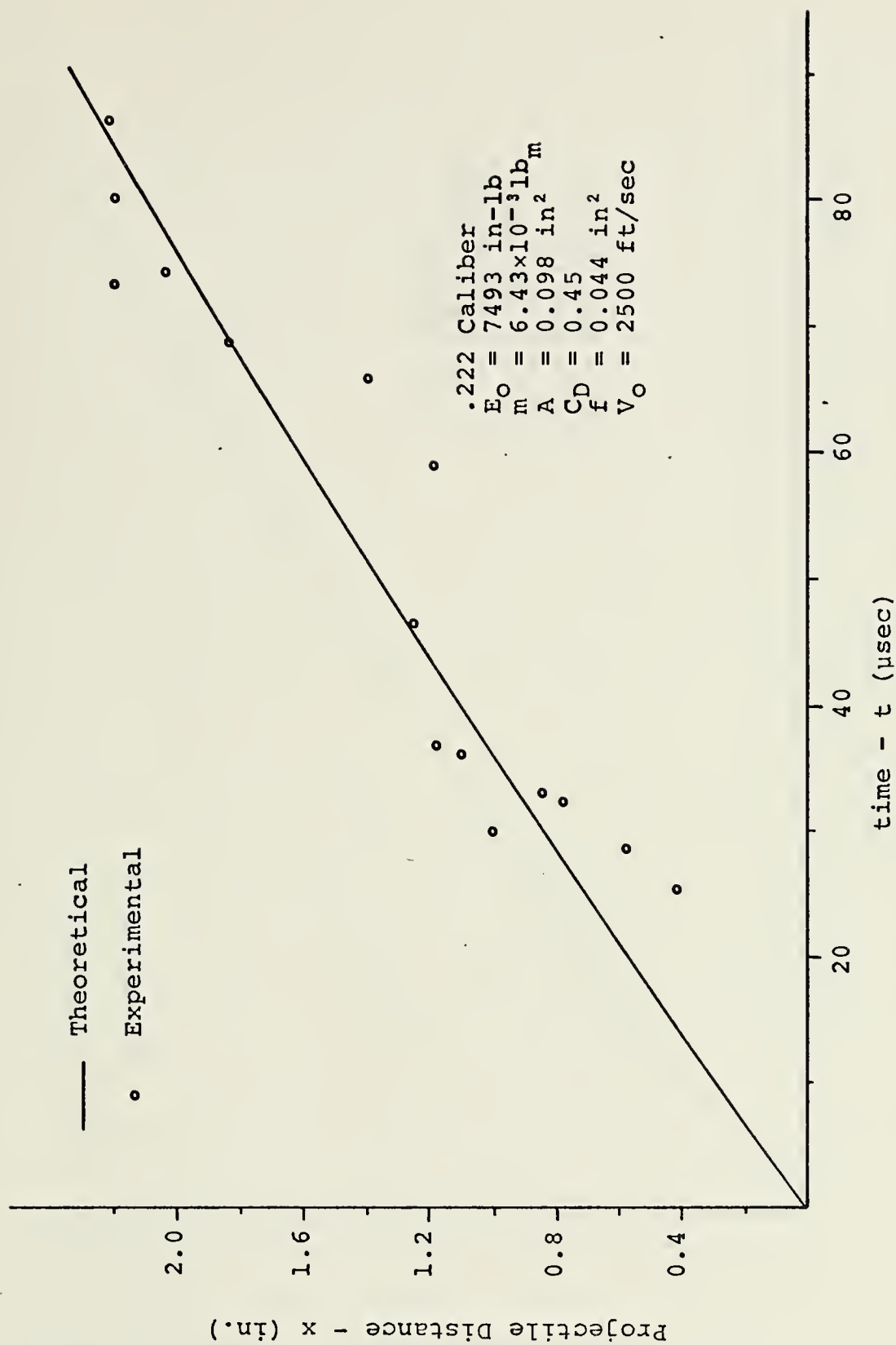


Figure 20. Projectile Distance in Fluid vs. Time,  $E_0 = 7493 \text{ in-lb}$



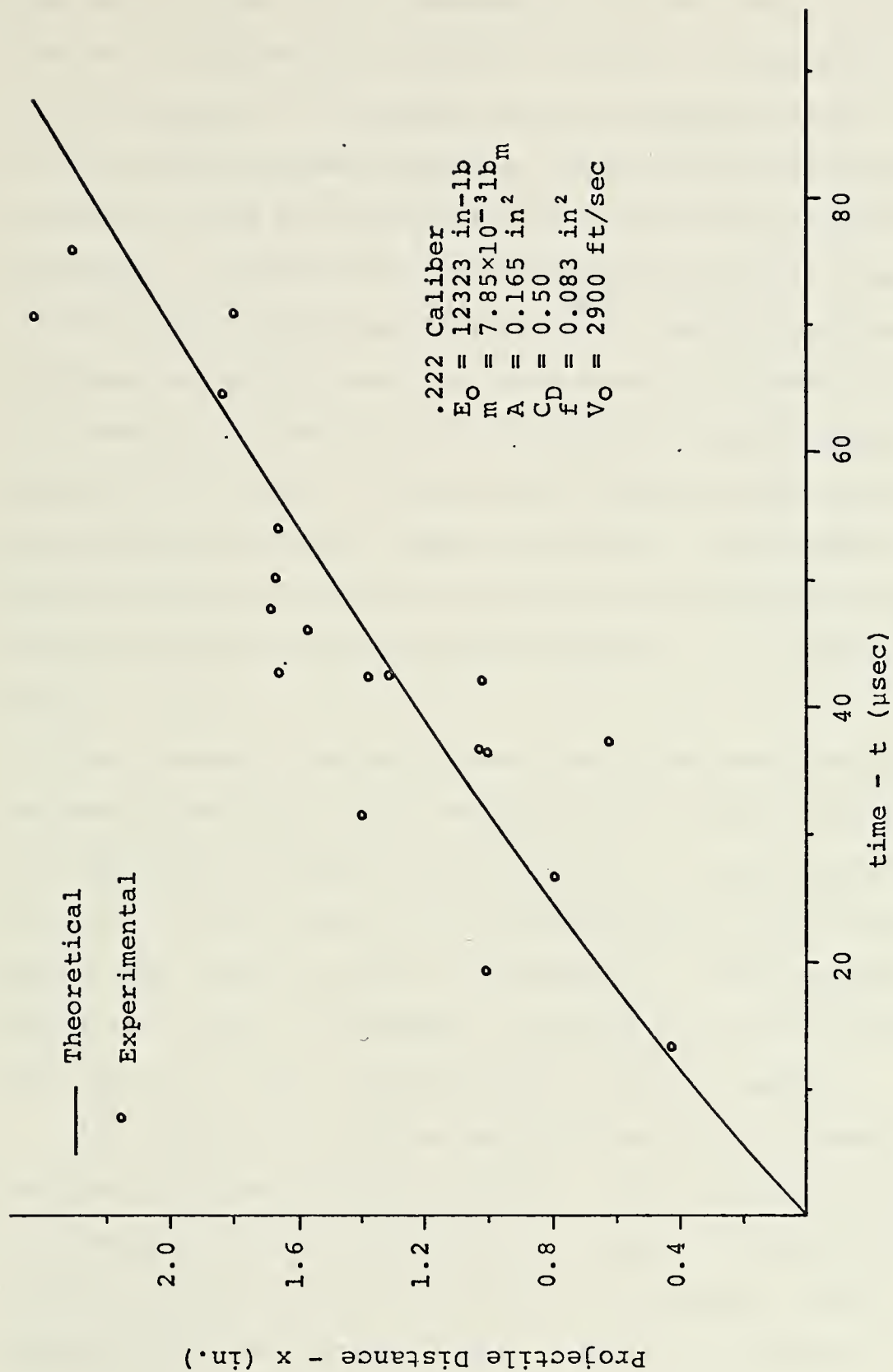


Figure 21. Projectile Distance in Fluid vs. Time,  $E_0 = 12323 \text{ in-lb}$



may be partially attributed to the rate of deformation of the projectiles. It is reasonable that the lead .22 caliber projectile deforms more rapidly than the .222 caliber jacketed projectile. It appears that the highest energy (12323 in-lb) projectile has reached a limit at which the projectile jacket and lead core cannot sustain the enormous stagnation pressure. No longer was the deformation similar to the two lower energy projectiles (figure 18). The drag coefficient, deformed projectile area and percentage of projectile velocity decay at a fixed distance for the two lower energy levels appears consistent. At the highest energy level, values for these variables do not appear consistent. When there is extensive deformation, as in the case of the highest energy level projectile, the assumptions appear to be overly simplified.

The concept of an equivalent flat plate area,  $f=C_D A$ , may be more advantageous than considering the drag coefficient and deformed projectile area separately. Also included in figure 4 is the value for the equivalent flat plate area,  $f$ , which best matches theory to experiment. This parameter reduces the number of dependent variables by one and describes the projectile drag characteristics with one number.

In reference 7, minimum impact velocities to penetrate various thickness plates are given. The experimental velocity decay data were extrapolated by theory to predict projectile velocities at the rear wall of the tank. These were compared with the minimum impact velocity to penetrate the



rear wall. After traveling the depth of the tank, 17 inches, the .22 caliber projectile ( $E_0 = 1600$  in-lb) was predicted to have a velocity of 0.394 ft/sec. Experimentally, the .22 caliber projectiles were found approximately six inches from the front wall where equation (4.2) predicts a velocity of 71 ft/sec. The .222 caliber projectiles with an energy of 7493 in-lb were predicted to have a velocity at the rear wall of 290 ft/sec, which was 32% of the minimum impact velocity required for penetration. The experiments with the .222 caliber projectiles at an energy of 7493 in-lb were the only test cases which made a noticeable dent but no penetration of the rear wall. The highest energy level projectiles were predicted to have a velocity of 105 ft/sec and there were no signs of projectile impact with the rear wall. These results seem to indicate that the exponential velocity decay is reasonable where projectile deformation is not extensive.

#### D. PRESSURE VERSUS RADIUS AND TIME

Figures 22, 23, 24 and 25 show theoretical predictions of the shock phase pressure pulse and the pressure profiles behind the shock at various times. Figure 22 is provided to demonstrate the order of magnitude of the shock pressure from initial impact until the shock becomes acoustic for an energy level of 1600 in-lb. The remainder of the pressure versus radius curves were limited to a range of 5 micro-seconds to 30 micro-seconds. This information was used to estimate pressure conditions which will be encountered when further experimental studies are undertaken to verify the theory.





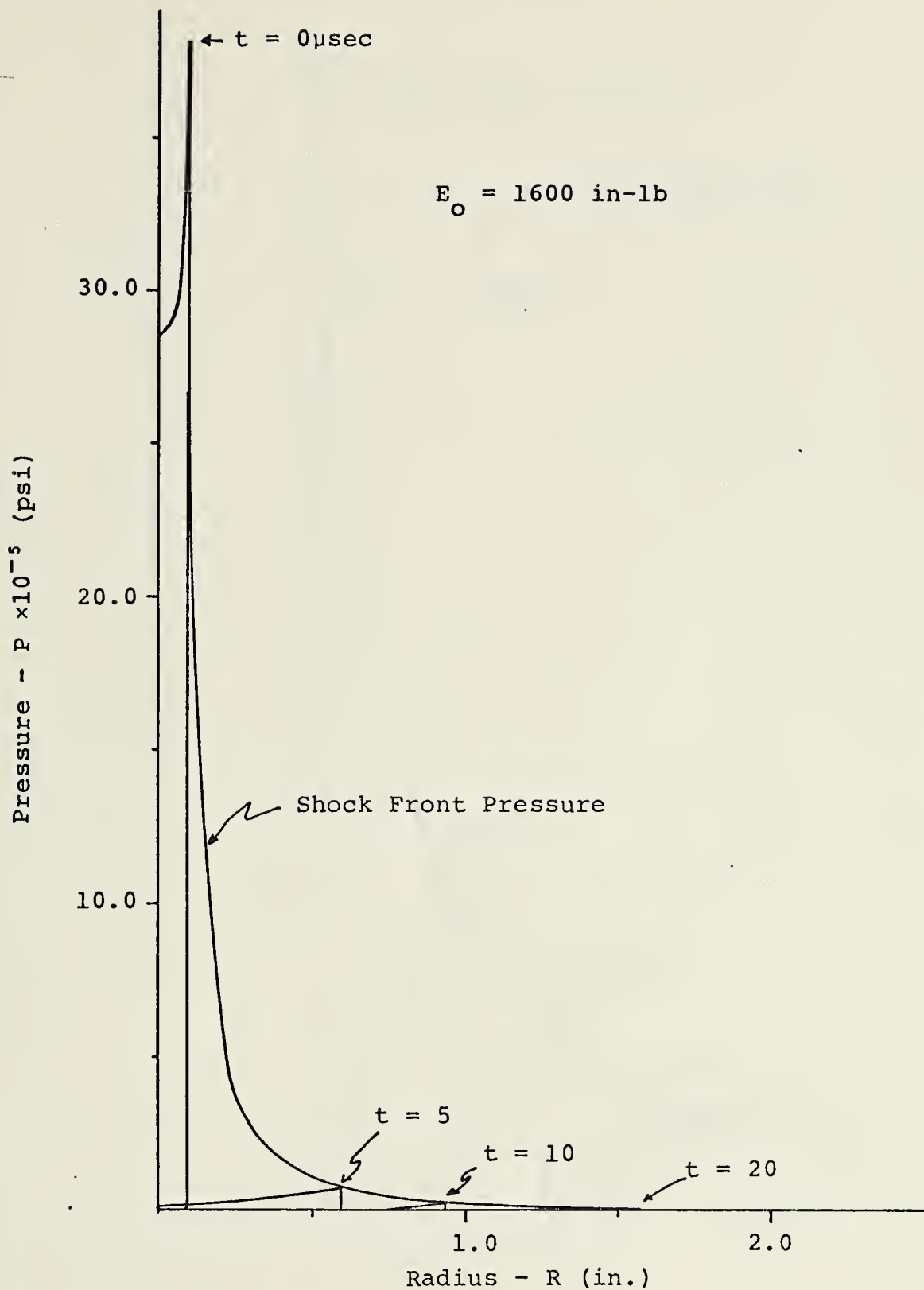


Figure 22. Pressure vs. Radius from Impact - Complete Profile,  $E_0 = 1600 \text{ in-lb}$



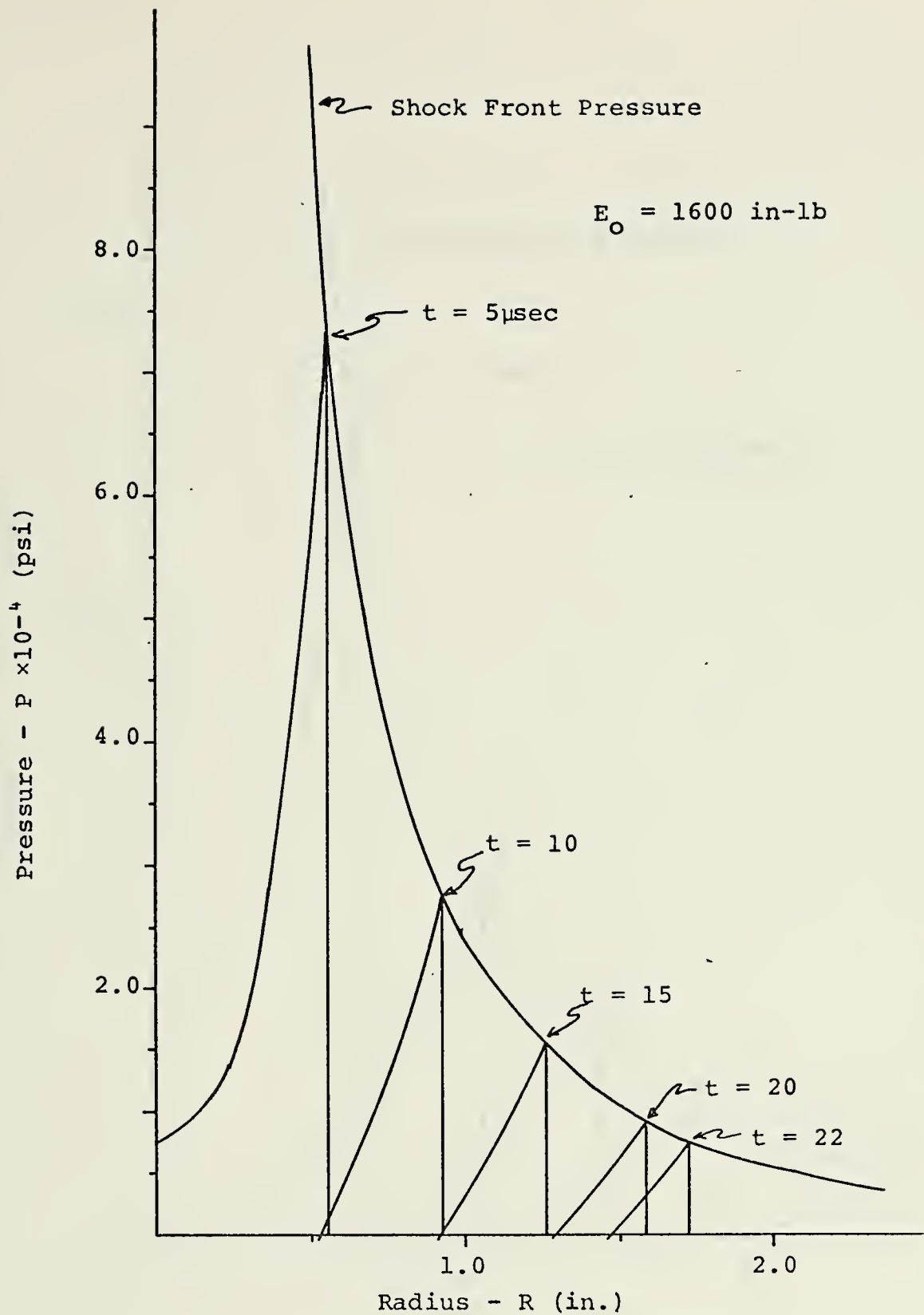


Figure 23. Pressure vs. Radius from Impact,  
 $E_0 = 1600 \text{ in-lb}$



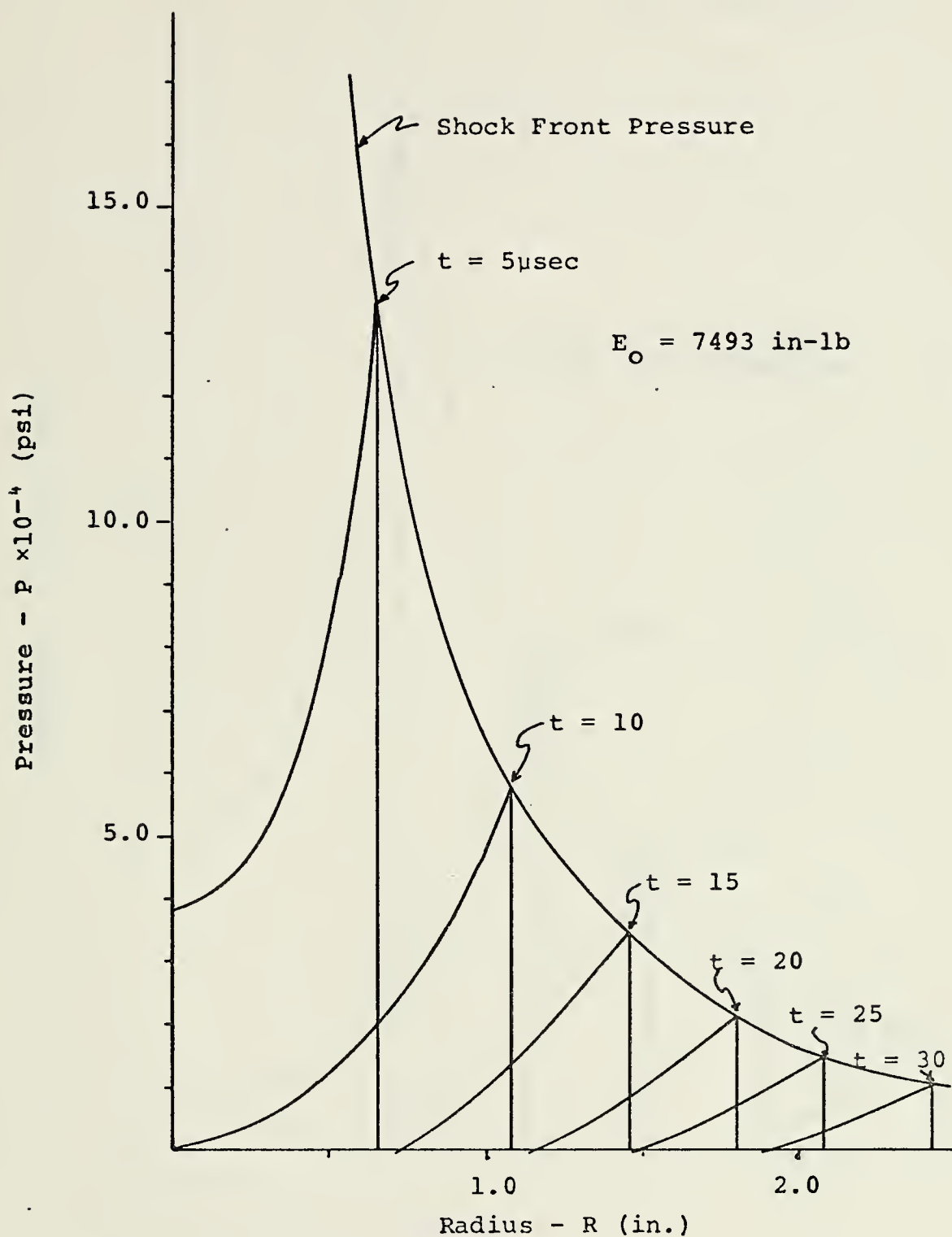


Figure 24. Pressure vs. Radius from Impact,  
 $E_0 = 7493 \text{ in-lb}$





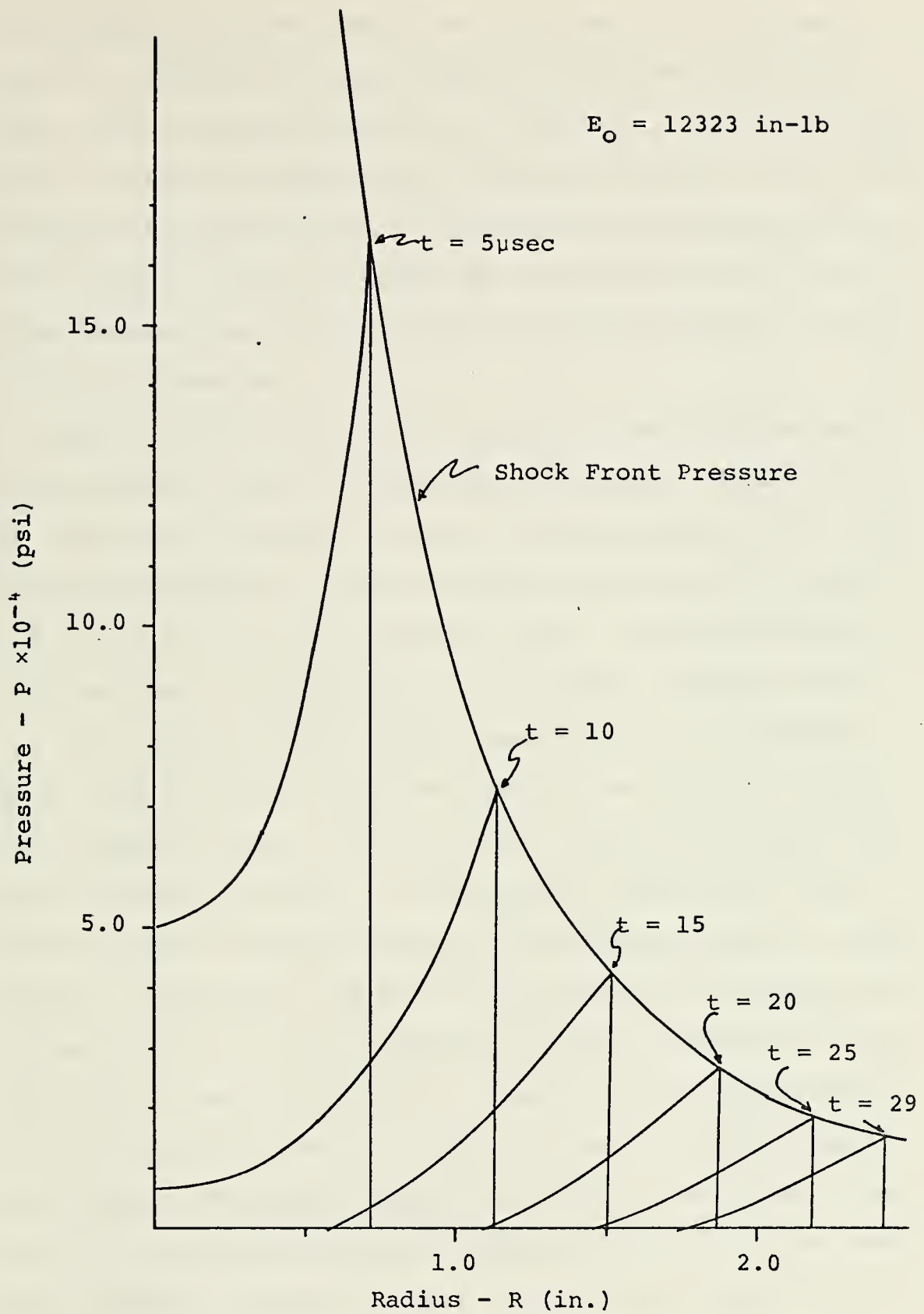


Figure 25. Pressure vs. Radius from Impact,  
 $E_0 = 12323 \text{ in-lb}$



The pressure profiles behind the shock were not plotted at negative pressures although negative pressures behind the shock front were predicted in the theoretical results. Since water is nearly incompressible, cavitation would occur as the pressures became negative. Cavitation has been observed on film records of similar hydraulic ram studies done at the Naval Weapons Test Center, China Lake and provided for the author by Lundstrom.

Immersion of pressure transducers in the fluid is being considered as a means of measuring pressures. Figures 26, 27 and 28 were plotted to estimate the magnitude of the pressures experienced at various distances from the front wall and the duration of the pressure pulse. The plots indicate the need for a transducer with a very fast response time.

It is expected that actual pressures will be somewhat lower than predicted, with the possible exception of blunt nose projectile data. There are two reasons for predicting lower pressure profiles. As explained earlier, the shock radius versus time data implied a weaker shock than the theoretical predictions. This was the result of the assumption in the theory that total impact energy was deposited in the fluid during shock formation. A weaker shock would result in correspondingly weaker shock pressures throughout the shock phase. The second reason pertains to the pressure profile as the shock Mach number approaches one. At lower shock Mach numbers, the assumptions of undisturbed fluid pressure in front of the shock being much less than at the shock



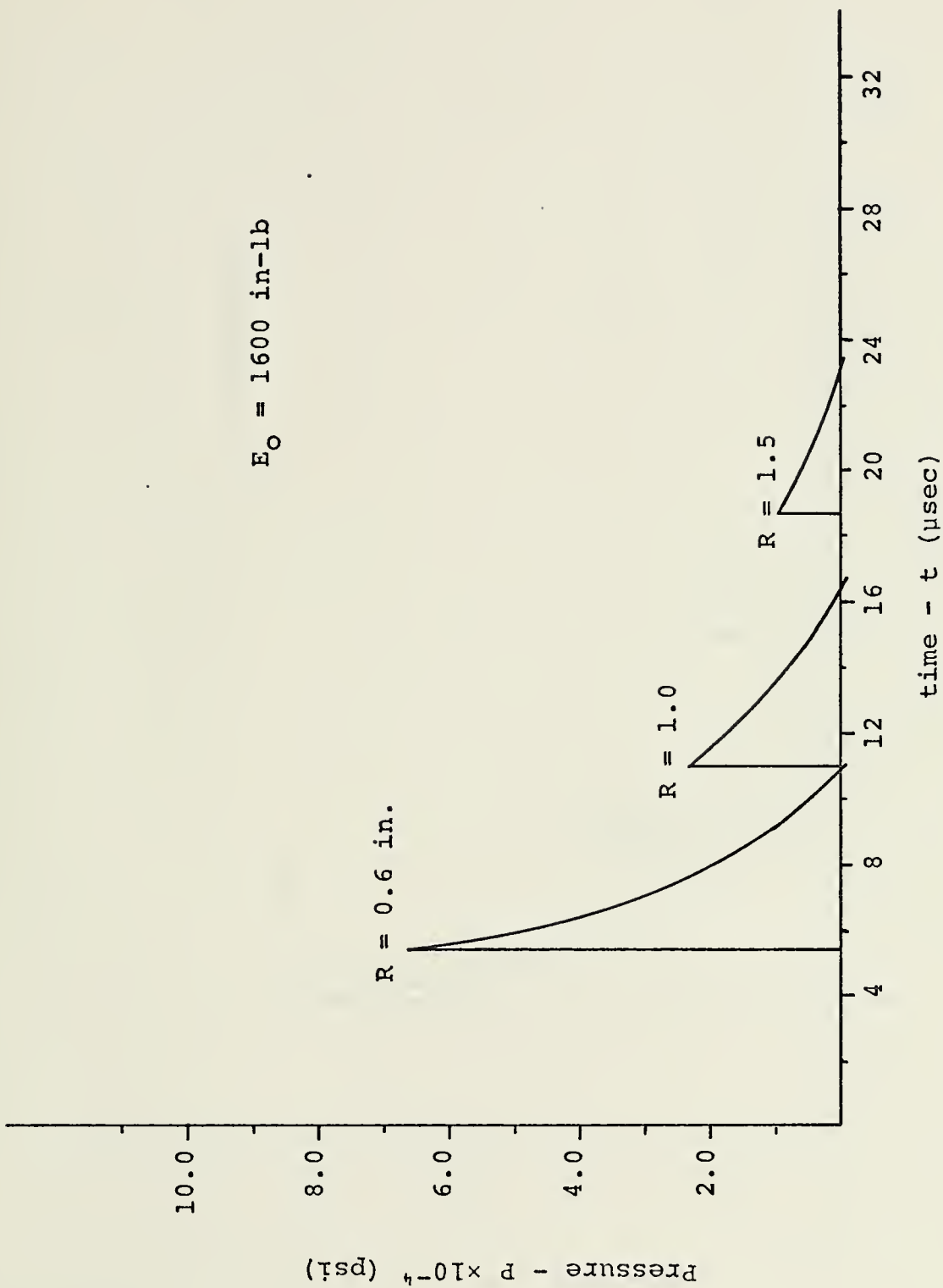


Figure 26. Pressure vs. Time for Three Radii,  $E_0 = 1600 \text{ in-lb}$



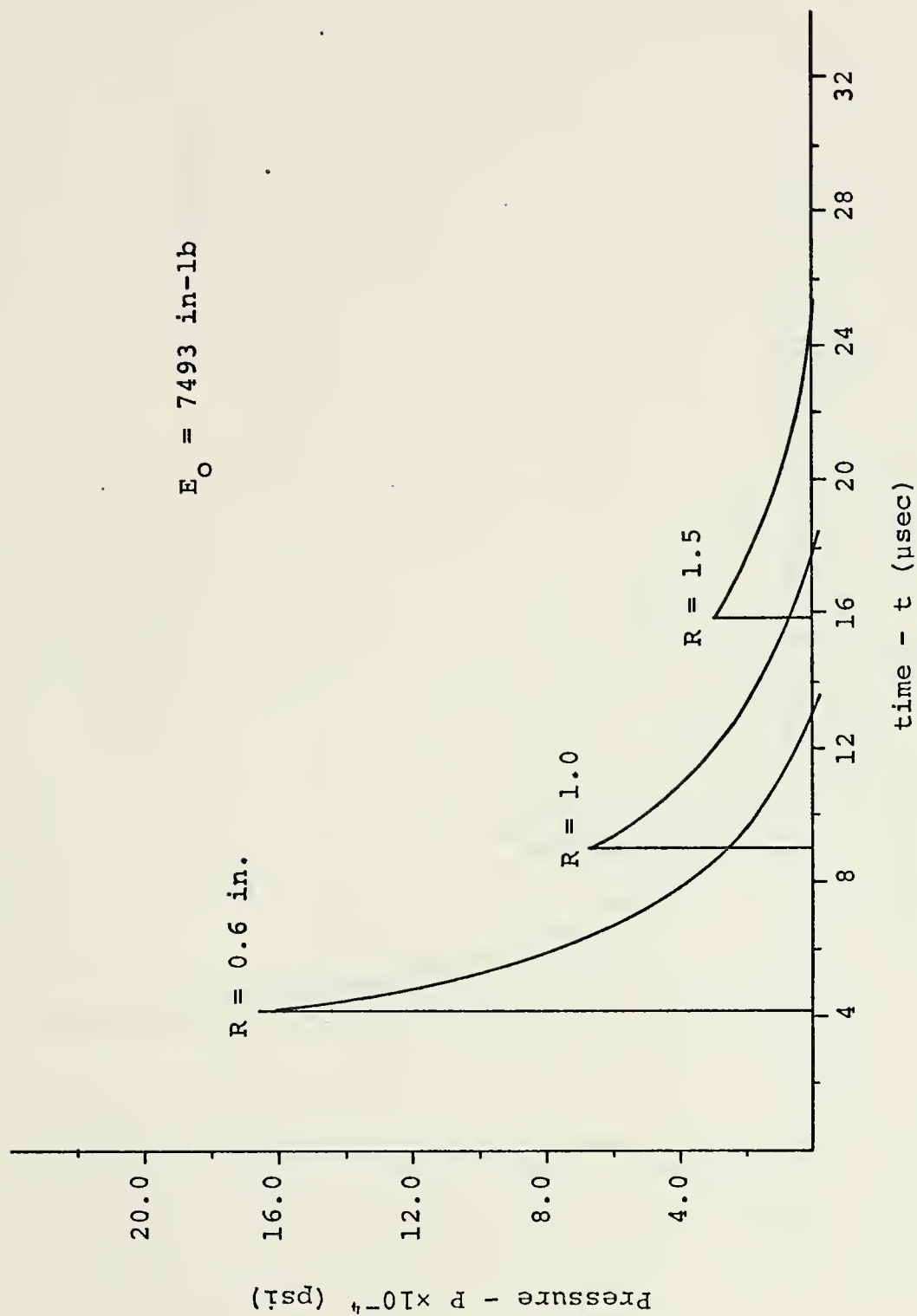


Figure 27. Pressure vs. Time for Three Radii,  $E_o = 7493 \text{ in-lb}$





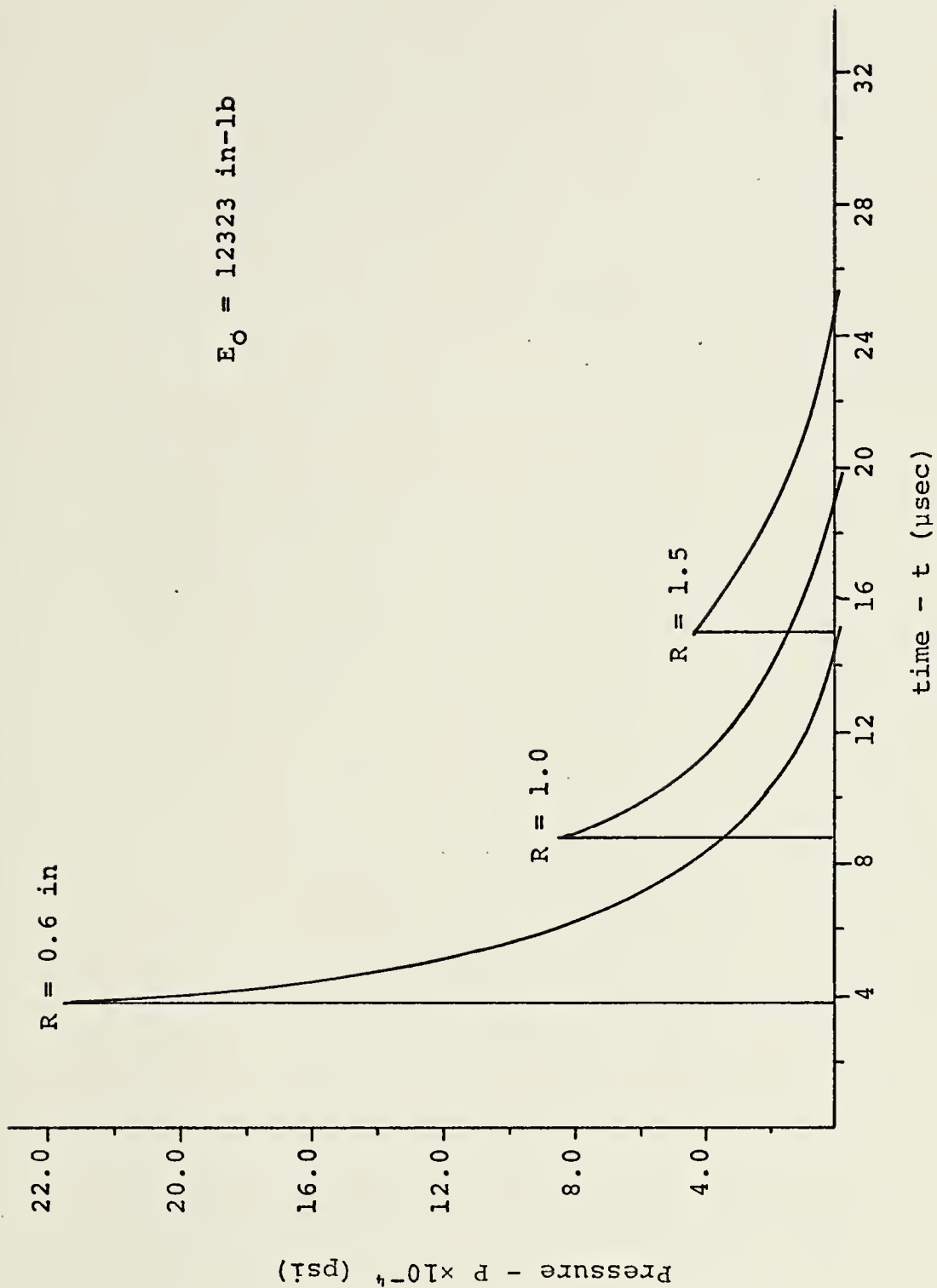


Figure 28. Pressure vs. Time for Three Radii,  $E_0 = 12323 \text{ in-lb}$



$(P_0 < P)$  will become invalid. This assumption should cause the theoretical predictions to be higher than experimental results.



## V. RECOMMENDATIONS

1. The scatter of the experimental data measuring shock radius versus time could be reduced by placing the fourth chronograph screen closer to the tank. New counters with high frequency, temperature compensated oscillators to provide a better time base are also recommended.
2. The ballistic range should be modified to provide the capability of firing higher energy projectiles. Shock radius versus time and projectile distance traveled in the fluid versus time should be studied at these higher energy levels.
3. Fluid pressure at and behind the shock should be compared with theory at various energy levels.
4. This study used lead or copper jacketed, lead core projectiles and no tumbling was observed. Further studies using steel jacketed projectiles should be completed to test for deviations from the data of this study. This information would provide the fuel cell designer with data typical of ballistic threats encountered in combat.
5. Strain gauges should be placed on the front wall specimens to determine the stresses incurred during the shock phase. Strain data could then be compared with SATANS computer code.
6. Higher energy projectiles which produce cracking or catastrophic failure of the front wall specimen should





be tested. These data would provide the designer with the critical energy level at which shock phase damage may result in an aircraft loss.



# COMPUTER PROGRAM

```

*****
*
* THIS PROGRAM CALCULATES THE FOLLOWING
* PART I
* 1. SHOCK RADIUS VERSES TIME
* 2. SHOCK MACH NUMBER VERSES TIME
* PART II
* 1. PRESSURE VERSE TIME AND RADIUS
* FROM IMPACT BEHIND THE SHOCK
* FOR A GIVEN FLUID AND IMPACT ENERGY,EO. THIS PROGRAM
* ASSUMES: SHOCK RADIUS IS PROPORTIONAL TO TIME TO THE
* C.8 POWER UNTIL ACCUSTIC, A POWER LAW DENSITY PROFILE
* BEHIND THE SHOCK, A STRONG SHOCK, ADIABATIC ACROSS
* THE SHOCK, THE UNDISTURBED FLUID PRESSURE IS ESSEN-
* TIALY ZERO, SPECIFIC INTERNAL ENERGY IN UNDISTURBED
* FLUID IS ESSENTIALLY ZERO.
*
*****

```

## SYMBOL DESIGNATION

```

EO= IMPACT ENERGY OF PROJECTILE (IN-LB)
CO= SPEED OF SOUND FOR FLUID (FPS)
RHOO= DENSITY IN UNDISTURBED FLUID (LB/FT3)
DC= INCREMENT OF NON-DIMENSIONAL RADILS, DELTA
    ZHETA
DELT= INCREMENT OF TIME (MICRO-SEC)
ET= ENERGY/VOL. = 2*EO/(R**3)
F1= NON-DIMENSIONAL PRESSURE AT THE SHOCK VS.
    SHOCK MACH NO.
DODM= DERIVATIVE OF NON-DIMENSIONAL PARTICLE
    VELOCITY W.R.T. SHOCK MACH NO. VS SHOCK
    MACH NO.
VS= SHOCK MACH NC.
X= PERCENT EO LOST AT ENTRY WALL

```

```

DIMENSION ET(20),PSI1(20),F1(20),VS(20),DODM(20)
1,RXMS(20),DRS(20),ARMS(20),DT(20),T(20),RE(20),
1RV(20),RDCD(20),XMS(20),RS(20),RPSI(20),RF(20)
DIMENSION TT(300),XM(300),R(300),F2(300),PSI2(300),
1DODM2(300),Q(300),C(100),F(2,20),P(2,20)
DIMENSION CONRS(300),SHOCV(300),TCFOR(300)
DIMENSION FOR(20)
DC 500 J=1,20
FOR(J)=0.0

```

500 CCNTINUE

N=18

READ (5,100) EO,CO,RHOO,X,DC,DELT

READ (5,101)(ET(I),I=1,N)

READ (5,101)(PSI1(I),I=1,N)

READ (5,101)(F1(I),I=1,N)

READ (5,101)(VS(I),I=1,N)

READ (5,101)(DODM(I),I=1,N)

WRITE (6,200) EO,CO,RHOO,X,DC,DELT

DC 15 I=1,N

15 WRITE (6,201) ET(I),PSI1(I),F1(I),VS(I),DODM(I)

PART I



```

C      PERCENTAGE OF INITIAL ENERGY DEPOSITED AND INITIAL
C      SHOCK RADIUS
C      E0=X*E0
      R0=(E0*32.2*144./ (RH00*C0*C0*2.*3.1416))**.33333
C
C      INITIAL VALUE OF ENERGY/VOL.
C      ETO=2.*E0/(R0**3.0)
C
C      INVERT INPUT ARRAYS FOR USE WITH INTERPOLATION
C      ROUTINE, PIF2
C
      DC 12 I=1,N
      J=N-I+1
      RE(I)=ET(J)
      RPSI(I)=PSI1(J)
      RF(I)=F1(J)
      RV(I)=VS(J)
12  RDDC(I)=DDDM(J)
C
C      INTERPOLATE FOR INITIAL VALUES AT SHOCK
C
      VSO=PIF2(ETO,RE,N,RV)
      F10=PIF2(VSO,RV,N,RF)
      PSI10=PIF2(VSO,RV,N,RPSI)
      DCDM0=PIF2(VSO,RV,N,RDDC)
C
C      COMPUTE INITIAL TIME FOR DISTANCE R0
C
      TC=R0/(C0*VSO*12.0)
C
C      ASSIGN SUBSEQUENT VALUES OF SHOCK MACH NO. AT WHICH
C      SHOCK RADIUS WILL BE COMPUTED
C
      DC 10 I=1,N
      IF (VSO-VS(I)) 1,2,2
1  GC TO 10
2  M=N-I+1
   XMS(1)=VSO
   GC TO 11
10 CONTINUE
C
C      COMPUTE SUBSEQUENT VALUES OF SHOCK RADIUS
C
11 RS(1)=R0
   DO 20 J=2,M
   XMS(J)=VS(I)
   RS(J)=(2.*E0 / (ET(I)) )**.3333
   I=I+1
20 CONTINUE
   K=M-1
C
C      COMPUTE DELTA TIME CORRESPONDING TO SHOCK MACH NO.
C      AND SHOCK RADIUS
C
      DC 30 I=1,K
      DRS(I)= RS(I+1)-RS(I)
      ARMS(I)=2./(XMS(I)+XMS(I+1))
30 DT(I)=DRS(I)*ARMS(I)/(C0*12.0)
   T(1)=T0
      DC 40 J=2,M
40 T(J)= T(J-1)+DT(J-1)
   WRITE (6,102)
   WRITE (6,103) E0
   WRITE (6,110)
C
C      PRINT SHOCK MACH NO. AND SHOCK RADIUS VS TIME
C
      DC 50 I=1,M
50 WRITE (6,111) T(I),XMS(I),RS(I)
100 FORMAT (6E10.0)

```



```

101 FORMAT (8E10.0)
102 FCRMAT (1H,77,39X, 'ENERGY',15X, 'FLUID' )
103 FCRMAT (29X,1E20.7)
110 FCRMAT (1H,77,39X 'TIME',17X,'MACH',17X,'RADIUS' )
111 FCRMAT (29X,3E20.7)
200 FCRMAT (77, 6E20.7)
201 FORMAT (15X,5E20.7)

```

## PART II

INITIALIZE VARIABLES AND ASSIGN VALUES USED WITH  
NCN-DIMENSIONAL PRESSURE DISTRIBUTION FUNCTION

```

BBB=T(M)*1.E06+1.05
L=BBB
TT(1)=0.0
XM(1)=XMS(1)
R(1)=R0
F2(1)=F10
PSI2(1)=PSI10
DCDM2(1)=DCDM0
Q(1)=3.*(PSI10-1.0)
B=-0.25
I=1.0/DC +1.05
C(1)=0.0
WRITE (6,301)
WRITE (6,302) TT(1),XM(1),R(1)
WRITE (6,303)
DC 60 J=2,N
60 C(J)=C(J-1)+DC

```

CCMPUTE NON-DIMENSIONAL AND DIMENSIONAL PRESSURE FOR  
INITIAL SHOCK RADIUS.

```

DC 70 J=1,I
F(1,J)=F2(1)+PSI2(1)*(C(J)**(Q(1)+2.0)-1.C)*(F2(1)/
1 PSI2(1)-B*(F2(1)+XM(1)*DCDM2(1)))/(Q(1)+2.0)
P(1,J)=F(1,J)*RHO0*CO*CO*XM(1)*XM(1)/(32.2*144.)
PUNCH 91,R(1),C(J),P(1,J)

```

70 CCNTINUE

```

K=1
JJ=1
SUM=0.0
CALL FORCE(FOR,C,P,R,I,JJ,K)
DC 501 J=1,I
SUM=SUM+FOR(J)
WRITE(6,304) C(J),P(1,J),F(1,J),FOR(J)
501 CCNTINUE
TCFOR(1)=SUM

```

ITERATION TO SOLVE PRESSURE, SHOCK RADIUS, SHOCK MACH  
NO. VS TIME

```

DC 80 K=2,L
TT(K)=TT(K-1)+DELT
IF (TT(K)-T0) 21,21,22
21 XM(K)=XM(1)
R(K)=R(1)
F2(K)=F2(1)
PSI2(K)=PSI2(1)
DCDM2(K)=DCDM2(1)
Q(K)= Q(1)
DC 55 J=1,I
55 P(2,J)=P(1,J)
PUNCH 92,R(K)
GC TO 80
22 X=TT(K)

```

INTERPOLATION OF INPUT DATA AND PART I DATA FOR  
VARIABLES IN PRESSURE FUNCTION





C

```

XM(K)=PIF2(X,T,M,XMS)
R(K)=PIF2(X,T,M,RS)
Y=XM(K)
F2(K)=PIF2(Y,RV,N,RF)
PSI2(K)=PIF2(Y,RV,N,RPSI)
DCDM2(K)=PIF2(Y,RV,N,RDCD)
Q(K)=3.*(PSI2(K)-1.0)
WRITE (6,301)
WRITE (6,302) TT(K),XM(K),R(K)
WRITE (6,303)
DC 90 J=1,I
F(2,J)=F2(K)+PSI2(K)*(C(J)**(Q(K)+2.0)-1.0)*(F2(K)/
1 PSI2(K)-8*(F2(K)+XM(K)*DCDM2(K)))/(Q(K)+2.0)
P(2,J)=F(2,J)*RHOO*CO*CO*XM(K)*XM(K)/(32.2*144.)
PUNCH S1,R(K),C(J),P(2,J)
90 CCATINUE
JJ=2
SUM=0.0
CALL FORCE(FOR,C,P,R,I,JJ,K)
DC 502 J=1,I
SUM=SUM+FOR(J)
WRITE(6,304) C(J),P(2,J),F(2,J),FOR(J)
502 CONTINUE
TCFOR(K)=SUM
80 CONTINUE
WRITE(6,305)
CALL CONVER(R,XM,TCFOR,TT,L)
91 FORMAT (3E15.5)
92 FORMAT (1E15.5)
301 FORMAT (1H,/,36X,'TIME',17X,'MACH',17X,'RADIUS' )
302 FORMAT (29X,3E20.7)
303 FORMAT (1H,/,39X,'R/RS',17X,'P',17X,'F',19X,'FORCE')
304 FORMAT (29X,4E20.7)
305 FORMAT (1H,/,36X,'TIME',17X,'VELC',17X,'RADCLIS',17X,'T
10 FORCE')
END
FUNCTION PIF2 (X,XLIST,N,FLIST)

```

C  
C  
C

```

SECOND ORDER INTERPOLATION
DIMENSION XLIST (100), FLIST (100)
BLIF (P,Q,R,S,T) = ((Q-P)*(S-T)/(R-Q)+S)
IF (X-XLIST(N)) 2,1,1
1 I = N-1
GO TO 5
2 IF(X-XLIST(1)) 4,4,6
4 I = 1
5 K = 1
GO TO 30
6 K = 2
7 DO 8 I = 1,N
IF (X-XLIST(I)) 9,9,8
8 CCNTINUE
I=N
9 I = I-1
30 BLIF1 = BLIF(X,XLIST(I),XLIST(I+1),FLIST(I),FLIST(I+1)
1)
10 IF (K-1) 11,11,12
11 PIF2 = BLIF1
RETURN
12 IF((I+2)-N) 13,13,16
13 IF ((I-1)-1) 15,14,14
14 IF (ABS(XLIST(I-1)-X)-ABS(XLIST(I+2)-X))16,15,15
15 L = I+2
GO TO 17
16 L = I-1
17 BLIF2 = BLIF (X,XLIST(I),XLIST(L),FLIST(I),FLIST(L))
PIF2 = BLIF (X,XLIST(I+1),XLIST(L),BLIF1,BLIF2)
18 RETURN
END

```



```

SUBROUTINE FORCE(FOR,C,P,R,I,JJ,K)
*****
*
* THIS SUBROUTINE COMPUTES THE FORCE ON THE ENTRY WALL
* DUE TO SHOCK PHASE FOR A FRONT WALL WITH A
* PRE-PUNCHED HOLE, I.E. PROJECTILE DOES NOT IMPINGE ON
* FRONT WALL UPON ENTRY. COMPUTES FORCE TO BE ZERO FOR
* PRESSURE FIELD OVER THE PRE-PUNCHED HOLE OR WHERE THE
* PRESSURE GOES NEGATIVE. THE PROGRAM ACCOMPLISHES THIS
* BY A STRAIGHT LINE APPROXIMATION BETWEEN PRESSURE
* DATA POINTS.
* RHRS= NON-DIMENSIONAL RADIUS OF PRE-PUNCHED HOLE
* S= SLOPE OF STRAIGHT LINE BETWEEN PRESSURE DATA
* POINTS
* RX= THE INTERCEPT OF R/RHRS, NON-DIMENSIONAL RADIUS,
* WHERE PRESSURE IS ZERO
* FCR(N)= FORCE(LB) FOR AN ANNULUS WHOSE OUTSIDE RADIUS
* IS C(N) AND INSIDE RADIUS IS C(N-1)
*
*****

```

```

DIMENSION FOR(20),C(100),P(2,20),R(300)
RHRS=.375/R(K)
IF(RHRS-1.) 100,25,25
100 IF(JJ-1) 1,1,2
1 DC 10 N=2,1
S=(P(1,N)-P(1,N-1))/4.
IF(P(1,N-1)) 3,4,4
3 IF(P(1,N)) 5,5,6
5 FCR(N)=0.0
GC TO 10
6 RX=(S*C(N-1)-P(1,N-1))/S
IF(RHRS.GT.C(N)) GC TO 43
IF(RX.GT.RHRS) GC TO 60
PH=S*(RHRS-C(N-1))+P(1,N-1)
FCR(N)=(.5*(P(1,N)-PH)+PH)*3.1416*(C(N)*C(N)-RHRS
1*RHRS)*R(K)*R(K)
GC TO 10
60 FCR(N)=P(1,N)*.5*3.1416*(C(N)*C(N)-RX*RX)*R(K)*R(K)
GC TO 10
4 IF(RHRS-C(N-1)) 40,40,41
40 FCR(N)=(.5*(P(1,N)-P(1,N-1))+P(1,N-1))*3.1416*(C(N)
1*C(N)-C(N-1)*C(N-1))*R(K)*R(K)
GC TO 10
41 IF(RHRS-C(N)) 42,43,43
42 PH=S*(RHRS-C(N-1))+P(1,N-1)
FCR(N)=(.5*(P(1,N)-PH)+PH)*3.1416*(C(N)*C(N)-RHRS
1*RHRS)*R(K)*R(K)
GC TO 10
43 FCR(N)=0.0
10 CONTINUE
RETURN
2 DC 20 N=2,1
S=(P(2,N)-P(2,N-1))/4.
IF(P(2,N-1)) 13,14,14
13 IF(P(2,N)) 15,15,16
15 FCR(N)=0.0
GC TO 20
16 RX=(S*C(N-1)-P(2,N-1))/S
IF(RHRS.GT.C(N)) GC TO 143
IF(RX.GT.RHRS) GC TO 160
PH=S*(RHRS-C(N-1))+P(2,N-1)
FCR(N)=(.5*(P(2,N)-PH)+PH)*3.1416*(C(N)*C(N)-RHRS
1*RHRS)*R(K)*R(K)
GC TO 20
160 FCR(N)=P(2,N)*.5*3.1416*(C(N)*C(N)-RX*RX)*R(K)*R(K)
GC TO 20
14 IF(RHRS-C(N-1)) 140,140,141

```



```

140 FCR(N)=(.5*(P(2,N)-P(2,N-1))+P(2,N-1))*3.1416*(C(N)
1*C(N)-C(N-1)*C(N-1))*R(K)*R(K)
GC TO 20
141 IF(RHRS-C(N)) 142,143,143
142 PH=S*(RHRS-C(N-1))+P(2,N-1)
FCR(N)=(.5*(P(2,N)-PH)+PH)*3.1416*(C(N)*C(N)-RHRS
1*RHRS)*R(K)*R(K)
GO TO 20
143 FCR(N)=0.0
20 CCNTINUE
25 RETURN
END

```

SLBRoutine CONVER(R,XM,TOFOR,TT,L)

C  
C  
C  
C

THIS SUBROUTINE CONVERTS VELOCITY AND RADIUS  
TO KM/SEC AND CM RESPECTIVELY

```

DIMENSION R(300),XM(300),TOFOR(300),CONRS(300),SHOCV(
1300),TT(300)
DC 510 II=1,L
CONRS(II)=R(II)*2.54
SHOCV(II)=XM(II)*4.9/3.281
WRITE(6,520) TT(II),SHOCV(II),CONRS(II),TCFCR(II)
520 FORMAT(29X,4E20.7)
510 CCNTINUE
RETURN
END

```



## LIST OF REFERENCES

1. Naval Weapons Center Technical Publication, 5227, Fluid Analysis of Hydraulic Ram, by E. A. Lundstrom, July 1971.
2. McDonnell Aircraft Engineering Methods Authorization, F65-76-555, Hydraulic Ram: A Fuel Tank Vulnerability Study, by R. N. Yurkovich, September 1969.
3. Handbook of Chemistry and Physics, 42nd ed., p. 2157, Chemical Rubber Publishing Co., 1960.
4. NASA Technical Note, NASA TN D-3143, Investigation of Characteristics of Pressure Waves Generated in Water Filled Tanks Impacted by High Velocity Projectiles, by F. S. Stepka, C. R. Morse, and R. P. Dengler, December 1965.
5. AIAA Paper No. 67-141, Shock Propagation in Solid Media, by G. C. Bach and J. H. Lee, January 1967.
6. McMillen, J. Howard, "Shock Wave Pressures in Water Produced by Impact of Small Spheres," Physical Review, v. 68, p. 198-208, 1 November 1945.
7. Soper, W. R., Hydraulic Ram Studies, M.S. Thesis, Naval Postgraduate School, Monterey, 1973.
8. Holm, D. P., Hydraulic Ram Shock Wave and Cavitation Effects on Aircraft Fuel Cell Survivability, M.S. Thesis, Naval Postgraduate School, Monterey, 1973.
9. Boeing Company Report No. D 162-10294-1, Hydraulic Ram, by R. G. Blaisdell, September 1970.





# INITIAL DISTRIBUTION LIST

	No. Copies
1. Defense Documentation Center Cameron Station Alexandria, Virginia 22314	2
2. Library, Code 0212 Naval Postgraduate School Monterey, California 93940	2
3. Chairman, Department of Aeronautics, Code 57 Naval Postgraduate School Monterey, California 93940	1
4. Professor A. E. Fuhs, Code 57Fu Department of Aeronautics Naval Postgraduate School Monterey, California 93940	2
5. Professor H. L. Power, Jr., Code 57Ph Department of Aeronautics Naval Postgraduate School Monterey, California 93940	6
6. Professor R. E. Ball, Code 57Ba Department of Aeronautics Naval Postgraduate School Monterey, California 93940	1
7. Captain James McNerney DDR & E Pentagon Department of Defense Washington, D. C. 20301	1
8. CDR Merlin L. Johnson Naval Air Systems Command Washington, D. C. 20360	1
9. CDR D. Hicks Naval Air Systems Command Washington, D. C. 20360	1
10. LT L. G. Kappel 7242 Rita Lane Cincinnati, Ohio 45243	2
11. Mr. Wallace K. Fung, Code 5114 Naval Weapons Center China Lake, California 93555	2



REPORT DOCUMENTATION PAGE		READ INSTRUCTIONS BEFORE COMPLETING FORM
1. REPORT NUMBER	2. GOVT ACCESSION NO.	3. RECIPIENT'S CATALOG NUMBER
4. TITLE (and Subtitle) Hydraulic Ram Shock Phase Effects on Fuel Cell Survivability		5. TYPE OF REPORT & PERIOD COVERED Master's Thesis March 1974
7. AUTHOR(s) Leslie George Kappel		6. PERFORMING ORG. REPORT NUMBER
9. PERFORMING ORGANIZATION NAME AND ADDRESS Naval Postgraduate School Monterey, California 93940		8. CONTRACT OR GRANT NUMBER(s)
11. CONTROLLING OFFICE NAME AND ADDRESS Naval Postgraduate School Monterey, California 93940		10. PROGRAM ELEMENT, PROJECT, TASK AREA & WORK UNIT NUMBERS
14. MONITORING AGENCY NAME & ADDRESS (if different from Controlling Office) Naval Postgraduate School Monterey, California 93940		12. REPORT DATE March 1974
		13. NUMBER OF PAGES 70
		15. SECURITY CLASS. (of this report) Unclassified
		15a. DECLASSIFICATION/DOWNGRADING SCHEDULE
16. DISTRIBUTION STATEMENT (of this Report)  Approved for public release; distribution unlimited.		
17. DISTRIBUTION STATEMENT (of the abstract entered in Block 20, if different from Report)		
18. SUPPLEMENTARY NOTES		
19. KEY WORDS (Continue on reverse side if necessary and identify by block number) Hydraulic Ram, Shock Phase, Cavity Phase, Fuel Cell Survivability, Projectile Velocity Decay in Liquid, Pressure Profiles Behind Shock in Liquid.		
20. ABSTRACT (Continue on reverse side if necessary and identify by block number) Hydraulic ram concerns the dynamic loading and catastrophic failure of liquid filled fuel tanks impacted by high speed projectiles. Hydraulic ram is divided into two phases: shock phase and cavity phase. The shock phase was studied. Theoretical predictions of shock radius versus time were compared with experimental results. The theory was found to be reasonably accurate for blunt shaped projectiles.		



## Block 20 - ABSTRACT (Cont.)

Included in the theory were predictions of shock pressure and pressure profiles behind the shock. Theoretical pressures are presented graphically but were not validated by experiment.

Velocity decay of the projectiles in the liquid was investigated and correlated with theory to provide information for further studies of the cavity phase.



DEC 75

24023

Thesis

151059

K1425 Kappel

c.1

Hydraulic ram shock  
phase effects on fuel  
cell survivability.

DEC 75

24023

Thesis

151059

K1425

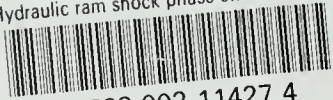
Kappel

c.1

Hydraulic ram shock  
phase effects on fuel  
cell survivability.

thesK1425

Hydraulic ram shock phase effects on fue



3 2768 002 11427 4

DUDLEY KNOX LIBRARY